Large-eddy simulations of the ice shelf-ocean boundary layer near the ice front of Nansen Ice Shelf, Antarctica

Ji Sung Na[1], Taekyun Kim[2], Emilia Kyung Jin[1*], Seung-Tae Yoon[3], Won Sang Lee[1], Sukyoung Yun[1],
Jiyeon Lee[1]

[1]Korea Polar Research Institute, Incheon, 21990, South Korea
[2]Jeju National University, Jeju, 63243, South Korea
[3]Kyungpook National University, Daegu, 41566, South Korea

Correspondence to: Emilia Kyung Jin (jin@kopri.re.kr)

Abstract. Ice melting beneath Antarctic ice shelves is caused by heat transfer through the ice shelf–ocean boundary layer (IOBL). However, our understanding of the fluid dynamics and thermohaline physics of the IOBL flow is poor. In this study, we utilize a large-eddy simulation (LES) model to investigate ocean dynamics and the role of turbulence within the IOBL flow near the ice front. To simulate the varying turbulence intensities, we imposed different theoretical profiles of the velocity. Far-field ocean conditions for the melting at the ice shelf base and freezing at the sea surface were derived based on *in situ* observations of temperature and salinity near the ice front of the Nansen Ice Shelf. In terms of overturning features near the ice front, we validated the LES simulation results by comparing them with the *in situ* observational data. In the comparison of the velocity profiles to shipborne LADCP data, the LES-derived strength of the overturning cells is similar to that obtained from the observational data. Moreover, the vertical distribution of the simulated temperature and salinity, which were mainly determined by the positively buoyant meltwater and sea-ice formation, was also comparable to that of the observations. We conclude that the IOBL flow near the ice front and its contribution to the ocean dynamics can be realistically resolved using our proposed method. Based on validated 3D-LES results, we revealed that the main forces of ocean dynamics near the ice front are driven by positively buoyant meltwater, concentrated salinity at the sea surface, and outflowing momentum of sub-ice shelf plume. Moreover, in the strong turbulence case, distinct features such as a higher basal melt rate ($0.153 \ \mathrm{m \ yr^{-1}}$), weak upwelling of the positively-buoyant ice shelf water, and a higher sea-ice formation were observed, suggesting a relatively high-speed current within the IOBL because of highly turbulent mixing. The findings of this study will contribute toward a deeper understanding of the complex IOBL-flow physics and its impact on the ocean dynamics near the ice front.

1 Introduction

The Antarctic Ice Sheet (AIS) is buttressed by floating extensions of land ice, called ice shelves (Rignot et al., 2013), which primarily control the AIS mass balance by hindering the flow of inland ice into the ocean (Holland et al., 2020). Iceberg calving, and basal melting are the key factors that can weaken the buttressing capacity of ice shelves (Liu et al., 2015; Smith et al., 2020).

The sub-ice shelf oceanic environment can be divided into two classes, namely the "cold-water cavity" (e.g., the Larsen C, Ross, Filchner–Ronne, and Amery ice shelves) and the "warm-water cavity" (e.g., the Getz and Totten ice shelves), depending on the amount of basal melting as well as ocean conditions (Gwyther et al., 2016; Joughin et al., 2012). In the cold-water cavity, shear force generated by the tides and sinking force of dense waters generated by brine rejection (e.g., high salinity shelf water (HSSW)) are the driving forces that cause basal melting (Davis and Nicholls, 2019; Yoon et al., 2020). In contrast, the intrusion of circumpolar deep water and melt-driven circulation near the grounding line are major causes of strong basal melting in the warm-water cavities (Holland et al., 2020; Jacobs et al., 1992).

Investigating the ice shelf–ocean boundary layer (IOBL), which is the boundary layer (meters to tens of meters) right beneath the ice shelf, is a complex problem because turbulent mixing and stably stratified ocean layer generated by basal melting both influence the IOBL characteristics (Begeman et al., 2018; Garabato et al., 2017). Various observational studies beneath ice shelves of Antarctica have been performed to observe the thermohaline characteristics and structures of the IOBLs as well as identify the ocean conditions beneath the ice shelves (Jenkins, 2010; Kimura et al., 2015). In the Larsen C ice shelf which is a cold-water cavity, a well-mixed boundary layer (20–30 m) was observed in both temperature and salinity, induced by a strong tidal forcing and a weak stratification. A moderate melt rate (1.9 m yr^{-1}) was observed, despite the low thermal driving due to the observed shear-driven turbulence (Davis and Nicholls, 2019). Similar melt rates for weak stratification were also observed beneath the Fimbul and Ross ice shelves (Arzeno et al. 2014; Hattermann et al., 2012). Moreover, the heat entrainment is prevented near the grounding line of the Ross ice shelf because of the strong density gradient between the meltwater and the denser continental shelf water in this region, yielding a low melt rate. (Begeman et al., 2018).

Positively buoyant sub-ice shelf plumes that are created near the grounding line and rise up along the ice shelf bottom can affect the stratification and heat entrainment within the IOBL because upper part of sub-ice shelf plumes is the IOBL (Hewitt, 2020; Holland and Jenkins, 1999). Since the sub-ice shelf plume modulates the IOBL characteristics with a strong turbulent mixing, the basal melt rate can be increased by weakening the stratification and enhancing the entrainment of the seawater from the outer region. As the sub-ice shelf plume generated by the HSSW in the cold-water cavities gets closer to the ice front, it flows outward, losing its buoyancy (Smithie & Jacobs, 2005).

Observational efforts of meltwater behavior and ocean circulation near the frontal region of the ice shelf demonstrate various mechanisms at different locations around Antarctica. In the frontal region of the Pine Island Ice Shelf, Garabato et al. (2017) revealed that the ascent of the meltwater outflow causes vigorous lateral export, affecting the settling of meltwater at depth. The intrusion of relatively warm surface waters and high basal melting near the ice shelf front was observed in the Ross

Ice Shelf (Hogan et al., 2011). Moreover, Malyarenko et al. (2018) suggested the existence of a "wedge" of fresher water in the Western Ross Sea and it is formed from meltwater near the ice shelf front. However, understanding of meltwater generation and behavior near the frontal region of the ice shelf is still poor, because the observation of sub-ice shelf environments is quite limited.

65

In contrast to Reynolds averaged Navier-Stokes model which provides time-averaged feature, high-resolution turbulence models such as the large-eddy simulation (LES) or direct numerical simulation (Gayen et al., 2016; McConnochie and Kerr, 2018; Mondal et al., 2019; Vreugdenhil and Taylor, 2019) can resolve the detailed eddy structures and quantify the momentum and heat fluxes near the wall boundary. Therefore, the LES for the IOBL flow is required to analyze the detailed IOBL structure and reveal fundamental information about the basal melting phenomenon occurring below the ice shelves (Jenkins, 2016; Vreugdenhil and Taylor, 2019). The LES has been successfully applied to investigate the role of turbulence in the ice–ocean interactions in Greenland (Carsey and Garwood, 1993; Denbo and Skyllingstad, 1996) and the Arctic Sea (Glendening, 1995; Skyllingstad and Denbo, 2001; Matsumura and Ohshima, 2015; Ramudu et al. 2018; Li et al. 2018). However, studies on the application of LES to the IOBL under a sub-ice shelf environment are limited due to lack of observations (Dinniman et al., 2016).

70

75

In this study, we performed LES experiments for the IOBL and ocean flow with neutrally buoyant sub-ice shelf plumes near the ice front. To include the thermohaline effect by sea-ice formation at the sea surface and basal melting at the ice-shelf base, surface fluxes in both temperature and salinity were used. The boundary conditions used in LES experiments were derived based on the *in situ* observation data—namely the conductivity–temperature–depth (CTD), lowered acoustic Doppler current profiler (LACDP) data, and automatic weather station (AWS) data—collected in front of the Nansen Ice Shelf (NIS), which is cold-water cavity, during the Antarctic expedition led by the Korea Polar Research Institute in January and February 2017. One of the main objectives of this study was to investigate the neutrally buoyant sub-ice shelf plume's impact on basal melting. Therefore, the target parameter in the LES experiments was turbulence intensity within the IOBL because the sub-ice shelf plume and its heat entrainment are related to basal melting via turbulent shear. Another objective was to validate our proposed methodology (domain configuration and boundary conditions) and the oceanographic properties simulated using the LES. Using the validated three-dimensional LES outputs, we quantified the distribution of melting at the ice-shelf bottom as well as the associated factors such as turbulent characteristics and flux changes within the IOBL.

80

85

Section 2 of this paper presents the governing equations (i.e., the Navier–Stokes equation and liquidus condition) for the oceanic flow with melting and freezing effects as well as a detailed explanation of the simulations. Section 3 presents the analysis of the LES simulation results to determine the IOBL characteristics—flow velocity, potential temperature, salinity, fluxes, and turbulence statistics. The major findings, future works, and implications of this study are summarized in Sections 4 and 5.

90

2 Methodology

2.1 CTD, LADCP observations

During the hydrographic survey by the icebreaking research vessel ARAON operated by the Korea Polar Research Institute, full-depth CTD and LADCP profiles were obtained in one-hour intervals from 14 February 2017 13:00 UTC to 15 February 2017 11:55 UTC at a single site in the Terra Nova Bay in front of the NIS. This survey was conducted to examine the vertical structures of the sub-ice shelf plume with temporal variations (grey lines in Figure 5). The exact location of the observations was 75.008 °S, 163.617 °E (Fig. 1b), located approximately 1 km away from the ice front. Because the LADCP data was incorrectly observed at the final casting, 24 CTD profiles and 23 LADCP profiles were used in this study. The CTD data were processed following the SBE recommended procedure (Sea-Bird Electronics, Inc., Bellevue, Washington, USA; 2014), and the LADCP data were processed using the methods introduced in Thurnherr (2004). This location for the observations is the coastal polynya region where strong katabatic winds cause extreme heat loss in the ocean, leading to sea-ice formation. Atmospheric properties such as wind speed, temperature, sensible heat and sea-ice formation were obtained using the AWS instrument on ARAON and are listed in Table 1. Based on the wind speeds and air temperatures in the AWS data acquired on ARAON, we calculated the sensible heat as well as the amount of sea-ice formation (Thompson et al., 2020). The detailed shipboard information and processing methods for the hydrographic data are described in Yoon et al. (2020).

2.2 Numerical model

To simulate the oceanic flow incorporating the effects of sea-ice formation and basal melting, the parallelized large-eddy simulation model (PALM, version 6–r4536) developed by Leibniz University was employed (Noh et al., 2009; Raasch et al., 2001). This model solves the non-hydrostatic, Boussinesq-approximated, filtered Navier–Stokes equations with buoyancy force, Coriolis force, and subgrid-scale (SGS) turbulent closure. The Boussinesq approximation can be applied to flows with negligible density variation. Furthermore, in the time integration, the time-difference formulas were computed using the third-order Runge–Kutta method. The 5th order upwind scheme was used to solve the flow advection (Wicker and Skamarock, 2002). The pressure was modeled using a Poisson equation, while the mass, momentum, potential temperature, and salinity conservations were governed by Eqs. (1)–(4) (Einstein summation convention), respectively.

$$\frac{\partial \overline{u_k}}{\partial x_k} = 0 \, , \tag{1}$$

$$\frac{\partial \overline{u_i}}{\partial t} + \frac{\partial \overline{u_i u_k}}{\partial x_k} = -\frac{1}{\rho}\frac{\partial \overline{\pi^*}}{\partial x_k} - \varepsilon_{ijk} f_j \overline{u_k} + \varepsilon_{i3k} f_3 \overline{u_{g,k}} + g\frac{(\rho_\theta - <\rho_\theta>)}{<\rho_\theta>}\delta_{i3} - \frac{\partial \tau^r_{ki}}{\partial x_k} \, , \tag{2}$$

$$\tau^r_{ki} = \tau_{ki} - \frac{1}{3}\tau_{jj}\delta_{ki}, \ \overline{\pi^*} = \overline{p^*} + \frac{1}{3}\tau_{jj}\delta_{ki},$$

$$\frac{\partial \overline{\theta}}{\partial t} = -\frac{\partial \overline{u_k \theta}}{\partial x_k} + \frac{\partial H_k}{\partial x_k} + Q_\theta \, , \tag{3}$$

$$\frac{\partial \bar{S}}{\partial t} = -\frac{\partial \overline{u_k} S}{\partial x_k} + \frac{\partial S_k}{\partial x_k} + Q_s ,$$ (4)

where u_k is the flow velocity, ρ is the seawater density, π^* is the dynamic pressure, ε_{ijk} is the Levi–Civita symbol, f is the Coriolis force for 75S ($-1.41 \times 10^{-4}\,\mathrm{s}^{-1}$), δ_{ij} is the Kronecker delta function, g is the gravitational acceleration, ρ_θ is the potential density, T is the absolute temperature, ν is the dynamic viscosity, τ'_{kj} is the Reynolds stress, θ is the potential temperature, p is the hydrostatic water pressure, p_0 is the reference pressure, and S is the salinity (Jackett et al., 2006). Additionally, Q_θ and Q_s are the external forcing of the source/sink terms—T and S, respectively. The overbars indicate that the values have been filtered over the grid volume. Combining these equations, the SGS turbulent kinetic energy (e) equation can be derived as follows:

$$\frac{\partial \bar{e}}{\partial t} = -\overline{u_k}\frac{\partial \bar{e}}{\partial x_k} - \tau_{ki}\frac{\partial \overline{u_i}}{\partial x_k} + \frac{g}{\theta_0}\overline{u'_3 \rho'_\theta} - \frac{\partial}{\partial x_k}\overline{\{u'_k(e + \frac{p'}{\rho_0})\}} - \varepsilon$$ (5)

where $= \frac{\overline{u'_i u'_i}}{2}$, and ε is the SGS dissipation rate.

The SGS stresses (τ_{ki}, H_k, and S_k) for the momentum, potential temperature, and salinity are parameterized as follows: (Maronga et al., 2015)

$$\tau_{ki} = \overline{u_k u_i} - \overline{u_k}\,\overline{u_i} = -K_m\left(\frac{\partial \overline{u_i}}{\partial x_k} + \frac{\partial \overline{u_k}}{\partial x_i}\right) + \frac{2}{3}\delta_{ik}\bar{e},$$ (6)

$$H_k = \overline{u_k \theta} - \overline{u_k}\,\bar{\theta} = \overline{u'_k \theta} = -K_h\left(\frac{\partial \bar{\theta}}{\partial x_k}\right), \quad K_h = \left(1 + 2\frac{l}{\Delta}\right)K_m ,$$ (7)

$$S_k = \overline{u_k S} - \overline{u_k}\,\bar{S} = \overline{u'_k S'} = -K_h\left(\frac{\partial S}{\partial x_k}\right),$$ (8)

$$\frac{\partial}{\partial x_k}\left[\overline{u'_k(e + \frac{p'}{\rho_0})}\right] = -\frac{\partial}{\partial x_k}\nu_e\frac{\partial \bar{e}}{\partial x_k}, \nu_e = 2K_m ,$$ (9)

$$\varepsilon = C_\varepsilon \frac{e^{3/2}}{l}, \quad C_\varepsilon = 0.19 + 0.74l,$$

$$K_m = C_m l\sqrt{\bar{e}} \quad \text{with empirical value } C_m = \text{constant} = 0.1, \text{ and } l = \min\left(1.8z, \Delta, 0.76\sqrt{\bar{e}}\left[\frac{g}{\rho_{\theta,0}}\frac{\partial \overline{\rho_\theta}}{\partial z}\right]^{-\frac{1}{2}}\right)$$

where K_m and K_h are the eddy diffusivities for momentum and heat; l is the turbulent mixing length which depends on height z (distance from the wall), grid spacing, and stratification; $\Delta = (\Delta x \Delta y \Delta z)^{(1/3)}$ is the length scale of the filter; and ρ_θ is the potential density. (the variables with prime are SGS variables). Because this SGS model and the coefficients are designed for a stably stratified boundary layer flow, it is suitable for resolving a stratified ocean flow with melting or freezing effect. However, the SGS fluxes can be incorrectly determined at a region where the flow becomes laminar, as this model assumes only a turbulent flow.

It is necessary to determine the ambient variables (θ_f and S_f) away from the ice shelf base and the interfacial variables (θ_b and S_b) near the ice shelf–ocean boundary to resolve the thermal and salinity changes caused by the freezing effect at the sea surface or the basal melting effect at the ice shelf–ocean boundary. Herein, we determined the ambient variables based on *in situ* CTD observations obtained 1 km away from the ice front (Figure 1b). To obtain the interfacial variables, we solved the conservation equations of heat and salt, along with the liquidus condition and turbulent transfer coefficients for heat and salt (Beckmann and Goosse, 2003; Vreugdenhil and Taylor, 2019).

$$c_w \rho_w \Gamma_\theta u_*(\theta_f - \theta_b) = \rho_i L_i m , \qquad (10)$$

$$\rho_w \Gamma_S u_*(S_f - S_b) = \rho_i S_b m , \qquad (11)$$

$$\theta_b = \lambda_1 S_b + \lambda_2 + \lambda_3 P , \qquad (12)$$

$$S_b = \frac{-\left(\lambda_2 + \lambda_3 P - \theta_f + \frac{L_i \Gamma_S}{c_w \Gamma_\theta}\right) + \sqrt{\left(\lambda_2 + \lambda_3 P - \theta_f + \frac{L_i \Gamma_S}{c_w \Gamma_\theta}\right)^2 - 4\lambda_1 \left(\frac{L_i \Gamma_S}{c_w \Gamma_\theta}\right) S_f}}{-2\lambda_1} , \qquad (13)$$

155 where m is the melt rate at the ice-shelf base or the freezing rate at the sea surface; the subscripts w and i refer to the parameters for water and ice, respectively. The parameters values are listed in Table 1. The friction velocity at the ice-shelf base was calculated from the simulated velocity field. We used 0.026 m s^{-1} as the friction velocity for the calculation of thermal and salinity fluxes induced by the sea-ice formation, although the effect of wind stress on the momentum was excluded to focus on the relationship between the sub-ice shelf plume and the development of overturning cell (counter-clockwise direction cell

160 observed in Figure 5a).

The fluxes for temperature and salinity, $q_{\theta *}$ and q_{S*} at the ice-shelf bottom were formulated by Monin–Obukhov similarity and interfacial values, θ_b and S_b obtained by resulting equation, Eq (13) (McPhee et al., 1987; Ramudu et al. 2018):

$$q_{\theta *} = \Gamma_\theta [\theta(z_1) - \theta_b] u_* , \qquad (14)$$

$$q_{S*} = \Gamma_S [S(z_1) - S_b] u_* , \qquad (15)$$

165 where z_1 is first node from the boundary; u_* is the friction velocity which is calculated using logarithmic law of the wall with the velocity at the first node and surface roughness (z_0); Γ_θ and Γ_S are the non-dimensional transfer coefficients of heat and salt, respectively, determined from the near-wall physics. Based on a high-resolution LES study on the heat and salt transfer coefficients, which are described as functions of the friction velocity and thermal driving, these coefficients, Γ_θ and Γ_S at the ice-shelf base were found to be 8 × 10^{-3} and 2.6 × 10^{-4} for basal melting, respectively (Vreugdenhil and Taylor, 2019). For the

170 sea-ice formation at the sea surface, the same coefficients (5.8 × 10^{-3} and 2 × 10^{-4}) used in a previous study on sea ice formation in polynyas were used, because the thermal driving in our study was comparable to that in the previous study (Heorton et al., 2017). These melting and freezing effects were applied at the first grid from the ice-shelf base or the sea surface. In this study, the melting or freezing effects at the vertical side of the ice front were not included.

2.3 Simulation description

175 In this study, we conducted four LES simulations of the turbulence intensity within the IOBL to reveal the influence of turbulence on IOBL characteristics. Using the masking method, an idealized ice shelf with a depth of 280 m was described at the upper-left part of the simulation domain to indicate the ice shelf depth near the front of the NIS (Briscolini and Santangelo, 1989; Stevens et al., 2017). Left (right) boundary was set to inflow (outflow) boundary condition. Moreover, initial conditions of velocity, temperature, and salinity were same to inflow boundary conditions. For zonal velocity, potential temperature, and

180 salinity, the inflow boundary condition was set to Dirichlet boundary conditions with temporally constant vertical profiles. The outlet boundary condition was determined to match the radiation boundary condition (similar to extrapolation), which

prevented numerical errors without rapid changes in the velocity and scalar properties. This radiation boundary condition at the outlet boundary allowed wave-like motions within the domain to pass through the boundary with only a small reflection. The cyclic boundary condition was applied to lateral boundaries, whereas the Neumann boundary condition for momentum was imposed on the top boundary condition. In other words, the wind affects the scalar (temperature and salinity) fluxes but not the momentum fluxes at the sea surface. Details on the simulation domain and the boundary conditions are presented in Fig. 1, which shows the target study region, observation points, and simulation domain with a schematic diagram for the oceanic flow alongside a sub-ice shelf plume. In this study, we used the theoretical profiles of velocity for describing the outflowing of the sub-ice shelf plume. Different turbulence intensities were described in four different vertical profiles of the zonal velocity and imposed as inflow conditions at the boundary of the domain. Based on the power-law assumption of turbulent boundary layer flow ($U = U_t \times (z/z_0)^{(1/n)}$), different velocity profiles (inset profiles in Figure 2) were composed using different power-law indices, n = 3 (weak turbulence), 4, 5 and 7 (strong turbulence) to simulate the turbulence intensity within the IOBL (Irwin, 1979; Kikumoto et al., 2017) (height z represents the vertical distance from the ice shelf base). A surface roughness (z_0) was 0.005 m (Gwyther et al., 2016). The freestream (geostrophic) velocity U_t was set as 0.06 m s^{-1} at 572 m depth, based on the *in situ* observations near the ice front. To explore the effects of sub-ice shelf plume on ocean dynamics without wind stress, inflow boundary condition for velocity was set to zero above 280 m depth and zero surface stress at the sea surface were used as the top boundary condition, whereas that below the ice shelf base (280 m) were used for the sub-ice shelf plume. At the start of the simulation, the initial profiles were imposed on the whole domain. The vertical profiles of the inflow boundary conditions for potential temperature and salinity were determined from the 24 CTD observations (Figure 5). The potential temperature at inflow boundary condition above 280 m depth and at a depth from 280 m to 570 m were set equal to the temperature at the sea surface (–1.9 °C) and to the average temperature (–2.06 °C), respectively. Below 570 m, inflow profile of potential temperature was set to averaged potential temperature in CTD observation. The averaged salinity values (obtained from CTD observation) were adopted as the inflow boundary condition of salinity. The simulation dimensions were 3,456 m × 3,456 m × 864 m in the x, y, and z directions, respectively. For the simulations, a grid of 288 × 288 × 144 cells was used with a 12 m horizontal grid and a 6 m vertical grid. The grid size and surface roughness were adopted based on a numerical study on high shear plume flow (Gao et al., 2019). We performed a grid sensitivity study to the optimal grid size for higher accuracy and less computational costs (Figure S1 in Supplementary), and found that a moderate grid resolution of 288 × 288 × 144 was suitable for resolving the turbulence with the parameterization of melting and freezing effects. The total simulation time required to reach the quasi-steady state was 96 hours. A random generator for small velocity perturbation was applied at depths from 30 to 800 m to quickly spin up the turbulence. In the model simulation, we configured two physical domains, i.e., the sub-ice shelf and open ocean regions. In the open ocean, the simulated ocean velocity, potential temperature, and salinity results were validated using the CTD and LADCP observational data. Subsequently, the flow characteristics of the IOBL flow beneath the ice shelf were investigated in detail.

3 Results

3.1 Quasi-steady ocean environment near the ice front

To confirm that the IOBL and oceanic flows approach a quasi-steady state, we plotted the time series of the friction velocities at the first grid below ice-shelf base (Figure 2). The total simulation time (96 h) was normalized by the large-eddy turnover time (t^*), which was calculated as the scale of overturning large eddy within the IOBL (IOBL depth) divided by the friction velocity. The friction velocities in the four LES cases showed significant fluctuations during the whole period, indicating that large-scale eddies exist beneath the ice shelf. The friction velocity fluctuations due to large-scale eddies shows a repetitive pattern. The averaged friction velocities after 14 t^* for n = 3, 4, 5, and 7 were 0.00169, 0.00208, 0.00255, and 0.00283 m s^{-1}, respectively (Ramudu et al., 2018). This difference is due to the different momentum entrainment by the turbulence intensity within the IOBL. We concluded that these IOBL flows approached a quasi-steady state after 14 t^* because averaged friction velocities for the four cases changed slowly enough. Table 2 presents these friction velocities and the large-eddy turnover times for the four cases. We calculated the time-averaged results within the last 3 t^* period for the later analysis to capture the averaged features of the flow without temporal variance.

Figure 3 illustrates the vertical sections (y = 1,728 m, domain center) of the zonal velocity, potential temperature, and salinity which are time-averaged in the final 3 t^* period to examine the spatial distributions of the flow structures and variables in two end-member cases (n = 3, n = 7) for turbulence intensity. In the open ocean region, the velocities for weak and strong turbulence cases (upper panel of Figure 3) exhibited similar patterns for the two overturning cells in the upper ocean region (0–280 m depth). Since we did not impose the wind effect at the top boundary, we can conclude that the development of the outer overturning cell is mainly induced by the downwelling (negative buoyancy flux) of the locally concentrated salinity as well as the shear stress induced by the momentum difference between the upper region and sub-ice shelf plume. Moreover, the development of the inner overturning cell is mainly due to the upwelling of the buoyant water and the downwelling of the salt flux. Thus, the inner overturning cell is stretched in the vertical direction, whereas the outer overturning cell is stretched in the horizontal direction. This is because driving forces of inner cell and outer cell were buoyancy force and shear force, respectively. The downwelling convection in which the two overturning cells share drives the sub-ice shelf plume down, moving the isopycnal line (280 m depth at initial state) near the ice shelf to a depth of approximately 350 m. Positive buoyancy at the left side (near the ice front) of the inner circulating cell originated from the meltwater created at the ice-shelf base near the ice front. In this study, we refer to this water as the "positively-buoyant ice shelf water (PISW). In contrast to the sub-ice shelf plume, which has a neutral buoyancy near the ice front, PISW has a strong buoyancy. Consequently, PISW is a major contributor to the formation of the inner overturning cell. Because the temperature of the sub-ice shelf plume is higher than the local freezing temperature at a depth of 280 m, basal melting occurs (Figure 7) and creates the PISW. At zonal distances from 1,280 to 1,600 m, this PISW mixes with the outer ocean and exhibits a temperature that is approximately 0.1 °C lower than the surface freezing temperature, affecting the sea-ice formation near the ice front (middle panel of Figure 3). As shown in the lower panel of Figure 3, the upwelling of PISW causes an upward movement of the isopycnal line (identified by potential

density). Except for the upper open ocean where overturning cells are dominant, the water column is stratified well below a depth of 350 m.

250   A noticeable difference between the two cases is observed near the ice front and beneath the ice shelf. At depths from 280 to 320 m (IOBL region), relatively high zonal velocity beneath the ice shelf is observed in the strong turbulence case (n = 7). After passing the ice shelf, this relatively high-speed current flows in a direction perpendicular to the ice front. In the weak turbulence case (n = 3), a relatively low velocity is observed beneath the ice shelf and the current rises after passing the ice shelf front. These momentum differences in the two cases mainly affect the magnitude and scale of the circulating cells near

255   the ice front. Another noticeable difference between the two cases is the different temperature and salinity in the upper ocean region. In the strong turbulence case, the increased friction velocity affects the basal melting rate and a large amount of PISW, leading to a low temperature and salinity in the upper ocean region.

To examine the sea-ice distribution and PISW effect on sea-ice formation, we illustrate the horizontal distributions of the 3 t^* time-averaged freezing rate (sea-ice formation) at the sea surface, as shown in Figure 4. Because the atmospheric forcing,

260   friction velocity, interfacial temperature, and interfacial salinity at the sea surface are the same in all the four cases, the difference in the freezing rate originates only from the ocean conditions. Although the amount of PISW is small in the weak turbulence case, most of its PISW is rising along the ice front owing to a low flow momentum within the IOBL. Otherwise, some of the PISW in the strong turbulence case is also rising along the ice front, but most of them are advected to the upper mixed layer in the open ocean region. As a result, different patterns of the freezing rate are observed in the two cases. In the

265   weak turbulence case, most of the freezing (sea-ice formation) is concentrated at the frontal region of the ice shelf, indicating a maximum freezing rate of 8.9 m yr^{-1}. Although a maximum freezing rate of 7.16 m yr^{-1} is observed right in front of the ice shelf in the strong turbulence case, the spatial-averaged freezing rate is higher than that in the weak turbulence case. An interesting point in the strong turbulence case is the heterogeneous pattern of the freezing rate in the meridional direction. This feature is strongly related to the PISW layer formed by the PISW upwelling (Figure S2). In the weak turbulence case, the

270   PISW upwelling occurs along the ice front edge, forming a strong and narrow PISW layer near the ice front with strengthened inner overturning cell. However, heterogeneous patterns of the freezing rate are observed in the strong turbulence case, because the PISW layer near the ice front is wide zonally with a weakened inner overturning cell, permitting the larger baroclinic disturbance caused by sloped isopycnals. This heterogeneous pattern of the freezing rate is comparable to the disturbance scale (2,066 m), as identified from the Rossby radius of deformation which represents the length scale the rotation effect is dominant.

275   This scale is obtained from the depth-averaged buoyancy frequency and depth between the sea surface and IOBL bottom.

3.2 Validation of simulation results

The CTD and LADCP observation data (grey lines in Figure 5) shows the existence of sub-ice shelf plumes, which exhibit lower temperatures than the surface freezing temperature. Above a depth of approximately 350 m, a well-mixed feature of potential temperature and salinity are observed, suggesting a strong mixing in this region. Two interesting observations were

280   obtained that are difficult to explain. One of them is the existence of relatively low-temperature freshwater (–1.96 °C, 34.65

psu) at a depth of 100 m (Figure 5b and 5c). Because of the sea-ice formation (latent heat and salt flux) at the polynya of the NIS region in late summer season, we suggest that the low-temperature freshwater is produced from the ice shelf base, and not from the sea surface. This feature can be explained by the PISW upwelling process which can be observed in LES results. It is observed that the PISW is advected to the open ocean region at 100 m depth in the potential temperature distribution at an instantaneous time of 21.8 t* (not shown). Another is the negative velocity (toward the ice front) above a depth of 300 m. It is a coherent feature because all the 23 LADCP observations indicated a similar feature. Because the direction of the katabatic winds is positive (away from ice front), it is not the cause of the negative velocity. We hypothesis that there is a large-scale overturning cell (counter-clockwise) caused by the shear force of the sub-ice shelf plume and downwelling by the salinity flux at the sea surface.

To validate our LES results and examine our hypothesis for large-scale overturning cell, we plotted the vertical profiles of the stream-wise zonal velocity, potential temperature, and salinity at a distance of 1 km away from the ice front and CTD and LADCP observations to compare the vertical distribution of the momentum and variables related to potential density (Figure 5) quantitatively. In terms of the velocity, the LES results simulate the development of the outer overturning cell well, having vertical profiles similar to those observed in the LADCP data, although the velocity gradient of LES results is less-sharp compared to that observed in the LADCP data. This mismatch between the LES results and the observations arises from the underestimated convection force (underestimated strength of overturning cells). The potential temperature and salinity profiles of these four LES results agree with the 24 CTD profiles, in terms of magnitude and depth of peak values. The difference in the potential temperature above a depth of 350 m also arises from the underestimated strength of the overturning cells. These LES experiments were initiated from an initial state with observation-constrained boundary conditions (grey lines in Figure 5) and the effects of basal melting, sea-ice formation, and outflowing momentum of sub-ice shelf plume. Therefore, the underestimation of convection force comes from the setup of boundary conditions and the resolving of these effects. However, we conclude that the LES results are consistent with the *in situ* observations for the oceanic environments such as the development of the overturning cells, similar vertical structure of temperature and salinity.

Because the velocity gradient between the freestream velocity at 572 m and the velocity at the sea surface is similar in all the cases, the velocity profiles of the LES results at 1 km away from the ice front are similar. However, the different turbulent intensities affect the different momentum transfer into the IOBL, resulting in different melt rate. Due to a difference in the melt rate, the magnitude of the potential temperature in the upper mixed layer in all the cases are significantly different: in the upper mixed layer, the potential temperature in the four cases are approximately –1.925, –1.93, –1.932, and –1.943°C. This difference is due to the amount of PISW created from the ice shelf base, not due to the differences in the advection of PISW, because the total potential temperature in the strong turbulence case is lower than that in the weak turbulence case (Figure 4). Similar features with the effect of PISW are also observed in the salinity profiles.

In the LES model, the filtered Navier–Stokes equation is solved with the modelled effect of small-scale eddies to reduce the computational costs. Therefore, the criteria for "small-scale" are important; these criteria are determined by the grid size in the LES model. To evaluate and validate the grid size and the parameterization of small-scale eddies, it is necessary to

confirm that the turbulence characteristics of the LES result are similar to the turbulence characteristics of the inertial subrange in which energy cascading occurs. We obtain the one-dimensional turbulence energy by integrating the inner product of the wavenumber and two-point correlation calculated along the single line in the y-direction. The one-dimensional turbulence energy spectra at a depth of 291 m (within the IOBL) in weak and strong turbulence cases are plotted in Figure 6. Moreover, we examined different zonal locations (x = 400, 800, 1200, 1600, 2000 and 2400 m) to observe a spatial transition of the IOBL flow. For the high wavenumbers which are comparable to the grid scale, the energy spectra slope of the LES results is slightly smaller than –5/3 slope of the Kolmogorov scaling in the inertial subrange. These are similar to –1 slope of the Batchelor regime, indicating that the resolved turbulence has anisotropic characteristics in high Schmidt number. For the weak turbulence case, spatial transition of turbulence energy at the IOBL region is observed. As the direction of the flow is away from the inflow boundary, the turbulence energy is gradually increased beneath the ice shelf. In the open ocean, turbulence energy are similar. For the strong turbulence case, the trend of energy spectra is similar to that for the weak turbulence case, except at x = 1,200 m. The highest turbulence energy is observed near the ice front (x = 1,200 m), showing high momentum transfer near the ice front edge.

3.3 IOBL characteristics in the sub-ice environment

The afore-mentioned analysis shows that the LES model adequately resolves the oceanic flow beneath the ice shelf with the thermohaline dynamics, such as IOBL dynamics, PISW upwelling and convective downwelling by the salt flux at the sea surface. Next, we explore the flow characteristics of the IOBL beneath the ice shelf using the LES results. Since we assumed a flat base of the ice shelf in this study, the buoyant force of PISW does not accelerate the PISW at the ice shelf base. Driving forces within the IOBL flow are the shear forces caused by the momentum of the inflow through the boundary and the stratification force (stabilizing force) caused by melting. In this section, we comprehensively analyze the oceanic flow characteristics to reveal the relation between the flow physics and melting patterns within the IOBL beneath the ice shelf.

Figure 7 illustrates the horizontal distributions of 3 t^* time-averaged meting rate at the ice shelf base. Evidently, different magnitudes of the melt rates are observed in the weak and strong turbulence cases. Except the magnitude of the melt rate, the overall trend in the two different turbulence cases is similar. In the region close to the inflow boundary and ice front, the melt rate is highest. Because the inflow boundary conditions are theoretical profiles, the transition for a fully developed (spatially quasi-homogeneous) IOBL flow is needed. As shown in Figure S3 in supplementary, turbulence intensities in the weak and strong turbulence cases are fully developed after 312 and 336 m distances, respectively. Therefore, we exclude the region with non-developed turbulence in the analysis. The spatially averaged values of melt rate in the two different turbulence cases are 0.092 and 0.153 m yr^{-1}, respectively, showing a 66 % difference in the melt rate near the NIS front. The melt rates obtained in this study are significantly lower compared to those reported by Wray (2019) (0.45–0.95 m yr^{-1}) and estimated via the Cryosat-2 satellite observation during 2010–2018 (1 ± 0.6 m yr^{-1}) at the NIS ice front region (Adusumilli et al., 2020). The difference in melt rates can be explained by a discrepancy between our thermal driving, 0.056 °C (2.116 °C – 2.06 °C) and the thermal

driving, 0.14 °C (2.0 °C – 1.86 °C) considered by the study of Wray (2019). In this study, only the effect of sub-ice shelf plume was considered, but the observations in summer season are likely affected by both intrusion of relatively warm Antarctic

350 surface water and the effect of sub-ice shelf plume, resulting in a difference in the thermal driving and melt rates. If the melt rate in this study is assumed to be 0.12 m yr^{-1} (averaged value of 0.092 and 0.153), we can estimate that 12–25 % of the total basal melting near the NIS front is due to sub-ice shelf plumes.

To observe and quantify the velocity structure within the IOBL in the strong turbulence case and the Ekman layer development, we plot depth profiles (meridional-averaged) of the velocities, turbulence intensity and horizontal momentum

355 flux beneath the ice shelf (Figure 8). At 280–400 m depths, the zonal velocities exhibits different structures for all the four cases. The strong turbulence case displays the smallest mean shear gradient but the largest turbulence intensity, whereas the weak turbulence case has opposing features. Since the turbulence kinetic energy production is proportional to the mean shear gradient and turbulent shear stress (Pope, 2000), the turbulent shear stress is the highest in the strong turbulence case, indicating that the turbulent shear stress produces a large portion of turbulent kinetic energy production. Due to high turbulent shear, a

360 strong frictional Ekman layer with negative meridional velocity (flows to the right of geostrophic flow) develops within the IOBL. Moreover, the frictional Ekman layer depths for the weak and strong turbulence cases are 11 and 17 m, respectively. These depths are comparable to the depths (11.9 and 19.6 m, respectively) estimated based on the friction velocity and Coriolis parameter (Coleman, 1990).

Figure 9 shows the vertical profiles of the vertical fluxes of momentum and heat beneath the ice shelf. As shown in Figure

365 S4 which depicts the vertical buoyancy flux profiles, the PISWs in both the weak and strong turbulence cases have a stabilizing effect because of their positive buoyant characteristics. Moreover, the PISW in the weak turbulence case exhibits a larger buoyant force than that in the strong turbulence case. Combining the regions, where the meltwater and its stabilizing effect dominate, with that where the turbulence-induced heat entrainment is vigorous (5 % of the maximum heat flux), the IOBL bottom is determined, since the IOBL is analogous to the atmospheric boundary layer (Derbyshire, 1990). This is, the IOBL

370 region was defined as the region where the thermodynamic changes induced by the basal melting at the ice shelf base are dominant. In the strong turbulence case, the vertical momentum flux is negative, and its maximum is located within the IOBL (IOBL bottom: 319 m depth). This implies that the momentum entrainment from the sub-ice shelf plume to IOBL is effective, resulting in a large heat entrainment. However, the depth of the maximum negative flux in the weak turbulence case is located at 347 m, i.e., slightly away from the IOBL. This difference causes difference in the heat flux magnitude at the PISW bottom.

375 Because the IOBL flow is quasi-steady, a similar temperature within the IOBL is maintained under heat entrainment from the sub-ice shelf plume and cooling effect of the PISW advection. The positive heat flux at 280–319 m depths and negative heat flux at 320–400 m depths are caused by the large-scale turbulence convection, showing the occurrence of heat entrainment from the sub-ice shelf plume and cooling effect of the PISW advection. The integrated area of heat flux represents the heat entrainment for the basal melting and PISW formation. The maximum positive heat flux for the weak and strong turbulence

380 cases are 138 and 213 W m^{-2}, respectively, with a 54% difference. This difference is comparable with that (66 %) in the melt

rate near the ice front, confirming that the basal melt rate is proportional to the amount of heat flux and entrainment, because of the flow advection penetrating the stratified IOBL.

4 Discussions

4.1 Ocean environment near the NIS front

385   In this study, we simulated the neutrally-buoyant, sub-ice shelf plume and the oceanic environment affected by this plume. The main findings and conclusions are summarized in Figure 10. First, we observe the development of two overturning cells near the ice front. The inner overturning cell is caused by the upwelling of the PISW along the ice front slope and downwelling at concentrated salinity flux (local salt maximum) induced by the sea-ice formation. The outer overturning cell is caused by outflowing momentum of sub-ice shelf plume. Second, we identify the role of turbulence within the IOBL. Notably, a higher

390   turbulence intensity results in a large amount of ice melting near the ice front. A high turbulence intensity causes a large momentum transfer, resulting in an increased melting and relatively high-speed currents within the IOBL. The large momentum causes the IOBL current (positive zonal velocity) to flow perpendicular to the ice front after it passes the ice shelf.

The horizontal scales of the overturning cells differ slightly for the weak and strong turbulence cases. The horizontal scale (492 and 408 m for the cases with weak and strong turbulence, respectively) of the inner overturning cell is calculated, based

395   on the locations of the local salt maximum (zonal distance = 1776 m and 1692 m for the case with weak and strong turbulence, respectively) at the sea surface. Because we observed the negative velocity after local salt maximum at the sea surface, positive velocity of sub-ice shelf plume, and downwelling of the salinity flux, we can conclude that an outer overturning cell exists. However, we cannot observe the exact horizontal scale of the outer overturning cell owing to the limitation of the domain scale in this study. Because the flow with the sub-ice shelf plume beneath the ice shelf is a backward-facing step flow (reattachment

400   flow with geometry), we can estimate the horizontal scale of the outer overturning cell based on the reattachment length (Rygg et al., 2011). For the oceanic flow at a high Reynolds number (2×10^6), we observe the development of the outer cell (5.3–8.4 h (h is geometry height)) and inner cell (1.3–1.5 h). As the ice shelf thickness is 280 m, we suggest a 364–420 m inner overturning cell and 1,484–2,352 m outer overturning cell.

PISW upwelling is important for the formation of modified Antarctic surface water and ocean circulation near the ice

405   front. In a previous study on the freshwater wedge in the Western Ross Sea (Malyarenko et al., 2018), freshwater layer at sea surface was observed. They hypothesized that this freshwater mainly originates from the sea ice melting, ISW outflow, and frontal ablation. The PISW upwelling and its accumulation observed in this study could evidentially support the "basal melting input" as a feasible wedge formation mechanism proposed by Malyarenko et al. (2018). If we consider the relatively warm Antarctic surface water with inclusion of frontal ablation in a future study, we can investigate and quantify the contributions

410   of the basal melting and frontal ablation in the freshwater input in the NIS region. In the study of meltwater outflow and its vertical structure by Garabato et al. (2017), they observed that the injection of the high-buoyancy, meltwater-rich glacially modified water triggers overturning via centrifugal instability near the ice front. For the vertical velocity of the PISW (Figure

S5), we observed a high positive velocity (0.04 m s^{-1}) near the ice front and a negative velocity (0.02 m s^{-1}) at the local salinity maximum. Given that approximately 0.02 m s^{-1} of the vertical velocity is observed at 1 km away from the ice front by Garabato

415   et al. (2017), our findings can support the ascent of meltwater outflow observed in this previously reported study. In contrast to centrifugal instability in the Pine Island Ice Shelf, we can demonstrate the symmetric instability in this study (Figure S6 and S7). This difference is caused by the different directions of the current near the sea surface and the exclusion of the katabatic wind effect.

4.2 Limitations of the LES experiments

420   As shown in previous LES simulation of the ice–ocean boundary (Ramudu et al., 2018; Vreugdenhil and Taylor, 2019), the LES model is a powerful tool for resolving the flow and its three-dimensional structures with the change of mass and energy, with a high accuracy and low computational cost. Therefore, employing the numerical approach such as a regional ocean model and the LES model is one of the best solutions for resolving the three-dimensional structures in the oceanic flow. Under these circumstances, we demonstrated one method for investigating the IOBL physics and ocean dynamics by

425   combining the numerical approach with observational data and theoretical profiles (power-law profiles with different turbulent intensity). In this study, we used the LES model with *in-situ* boundary conditions to expand the one-dimensional observation profile in the open ocean region to the three-dimensional flow-field in the open ocean and sub-ice shelf regions. Additionally, we set the interfacial values (θ_b, S_b) in the liquidus condition using ambient values (θ_f, S_f) obtained from the CTD observational results. In this study, to evaluate the applicability of our proposed method, we validated our results with observations, in terms

430   of overturning cell characteristics, vertical structures of temperature and salinity. In a future work, this proposed methodology will be validated using *in situ* sub-ice shelf observations made using advanced instruments such as hot water drilling, autonomous underwater vehicles, glider, etc. Moreover, the boundary conditions for the sub-ice shelf region, the effect of wind stress and salt flux changes due to precipitation and evaporation will be investigated for simulating the IOBL and overturning cells more realistically.

435   In Terra Nova Bay, the northeastward katabatic wind is dominant and it drives the along-front current (Guest, 2021; Malyarenko et al., 2019). If we included the wind effect at the sea surface, the horizontal mixing may be enhanced, advecting the fresh meltwater of the PISW layer near the ice front to the open sea. In terms of overturning cells, the strength and horizontal scale of the outer overturning cell may decrease, as the wind stress reduces the shear stress between the sea surface and the sub-ice shelf plume. The weakened outer cell, in turn, weakens the inner (secondary effect) cell. However, the strength and

440   scale of the inner overturning cell may be similar to that obtained in the present study, because the wind stress at the sea surface is imposed at the upper part (positive velocity region) of the inner overturning cell. In summary, if the wind stress effect is included, similar scale of the inner circulating cell and a decreased scale of the outer circulating cell near the ice front can be expected.

In this study, we did not include the melting or freezing effects at the vertical side of the ice shelf. Because thermal driving

445   at depth of 146 m on the vertical side of the ice shelf was almost zero, the effects of melting and freezing occurred below and

above 146 m depth, respectively. Because 146 m was almost near the center of the ice front, the total change in the temperature and salinity, because of the melting and freezing effects at the entire ice front, was not significant. However, this feature in the ice mass change at the ice front might be related to the shape of the ice front edge.

450   In terms of the frazil ice processes, we only considered the latent heat release and salt flux produced by the sea-ice formation at the sea surface. However, suspended frazil ice, formed by adiabatic cooling, can occur in the region of PISW upwelling at the ice front and upwelling of the sub-ice shelf plume (in this study, this upwelling occurred outside the study domain). The effects of the frazil ice dynamics (e.g. crystal growth rate, nucleation, and concentration) on the sea surface or ice shelf water (PISW and sub-ice shelf plume) should be investigated, because the change in plume characteristics as well as the temperature and salinity are strongly related to the frazil ice dynamics (Galton-Fenzi et al., 2012; Rees Jones and Wells,

455   2018). Because the inclusion of suspended frazil ice affects the increased plume velocity and decreased plume density, the upwelling of the PISW can be strengthened. This increases the strength of the inner overturning cell. Owing to a high plume velocity and decreased plume density, only a few precipitations of frazil crystals within the PISW occur at the vertical side of the ice front. However, if the ice-front geometry is modified through an increased frazil ice formation by the freshwater wedge formation, precipitation on the modified geometry might increase, exhibiting a nonlinear effect on the change in the ice-shelf

460   geometry (Smedsrud and Jenkins, 2004).

In this study, we employed theoretical power-law profiles of the velocity, which exhibit different turbulence intensities, because observational data on the vertical structures beneath the ice shelf are rarely available. In the flux Richardson number in Table 2, the relationship between the stratification and turbulent mixing is not clear, even though we imposed different turbulence intensities. This implies that the negative feedback (enhanced buoyancy fluxes) of the PISW increases as the

465   turbulence intensity and its entrainment increases. In this study, we performed a preliminary assessment of the oceanic structures in a sub-ice shelf environment. The constant model coefficient (C_m) in the SGS model is applied in the IOBL flow near the wall and the flow within the sub-ice shelf plume to reduce the computational costs. In future studies, corrections to the coefficients will be required, based on high-resolution studies of near-wall turbulence. The main findings of this study can be used for understanding the IOBL physics and meltwater behavior near the sub-ice shelf cavity. If direct observational data

470   for the IOBL flow structures and turbulence characteristics in the sub-ice shelf environment can be obtained, then this study can be improved by comparing LES results to observations, and by introducing corrections into the ambient values and transfer coefficients for potential temperature and salinity. Other important factors that were not included in this study should be addressed and investigated in future studies such as the effect of ice shelf bathymetry (shape and slope) and surface roughness on the turbulence characteristics, temporal variability of the sub-ice water plume, wind stress effects, and consideration of the

475   melting at vertical side of the ice front. A better understanding of the relationship between afore-mentioned factors and the IOBL physics with basal melting will help in improving the parameterizations (e.g. vertical mixing within the IOBL and sea-ice formation and behavior) in the regional ocean model (e.g. ROMS and MITGCM).

5 Conclusions

480   We successfully simulated the IOBL flow with a sub-ice shelf plume, the melting effect beneath the NIS, and the freezing effect at the sea surface using a LES model and boundary conditions based on *in situ* observations. Since the inflow profile beneath the ice shelf are difficult to observe in *in situ* observation, we assumed the theoretical power-law profile to describe the different turbulence intensities. The flow simulated for a period of 96 h reached a quasi-steady state after 14 t^* (69 h and
485   55 h for the cases with weak and strong turbulence), exhibiting a large variance and repetitive pattern with temporal convergence of friction velocity. To validate the LES results for the four different turbulence intensities, the simulated zonal velocity, potential temperature, and salinity were compared with the 24-h CTD and LADCP observational data obtained near the NIS in the Terra Nova Bay of the western Ross Sea, during a 2016–2017 shipboard survey. The simulation results are consistent with the observations considering the development of two overturning cells and thermohaline properties.

    The different turbulence intensities in the IOBL flow beneath the ice shelf resulted in significantly different melting
490   features and flow dynamics. With increased friction velocity, the melt rate in the strong turbulence case increased by 66 % compared to that in the weak turbulence case, maintaining the stratification intensity (similar flux Richardson number). In the strong turbulence case, distinct features such as higher basal melting (0.153 m yr^{-1}), weak upwelling of the PISW, and a larger sea-ice formation were observed, suggesting a relatively high-speed current within the IOBL because of a highly turbulent mixing. Comparing with the observations, we estimated that 12–25 % of the total basal melting near NIS front is caused by
495   the sub-ice shelf plumes. We observed that the sub-ice shelf plume, PISW upwelling, and downwelling of concentrated salinity flux compose two overturning cells near the ice front.

Data availability

The numerical model, PALM 6.0 (Rev:4552M) used in this study is available at (https://palm.muk.uni-hannover.de/trac). Detailed model configurations with melting effect parameterization are described in detail in method section. The data used
500   are all publicly available and can be found via the relevant citations.

Acknowledgments

This work was sponsored by a research grant from the Korean Ministry of Oceans and Fisheries (KIMST20190361; PM21020).

Competing interests

The authors declare that they have no conflict of interest.

Author contributions.

JSN, EKJ, WSL conceived the study. JSN modified PALM model and the code of surface fluxes for ice melting, and JSN conducted a suite of simulations. JSN, TK, STY, SY, and JL conducted CTD, LADCP observation and its analysis. JSN and EKJ wrote the manuscript with contributions from all authors.

References

510 Adusumilli, S., Fricker, H. A., Medley, B., Padman, L. and Siegfried, M. R.: Interannual variations in meltwater input to the Southern Ocean from Antarctic ice shelves. Nat. Geosci., 13(9), 616–620 doi:10.1038/s41561-020-0616-z, 2020.

Arzeno, I. B., Beardsley, R. C., Limeburner, R., Owens, B., Padman, L., Springer, S. R., Stewart, C. R. and Williams, M. J.: Ocean variability contributing to basal melt rate near the ice front of Ross Ice Shelf, Antarctica. J. Geophys. Res. Oceans, 119(7), 4214–4233, doi:10.1002/2014JC009792, 2014.

515 Begeman, C. B., Tulaczyk, S. M., Marsh, O. J., Mikucki, J. A., Stanton, T. P., Hodson, T. O., Siegfried, M. R., Powell, R. D., Christianson, K. and King, M. A.: Ocean Stratification and Low Melt Rates at the Ross Ice Shelf Grounding Zone, J. Geophys. Res. Oceans, 123(10), 7438–7452, doi:10.1029/2018JC013987, 2018.

Briscolini, M., and Santangelo, P.: Development of the mask method for incompressible unsteady flows. Journal of Computational Physics, 84(1), 57–75, doi:10.1016/0021-9991(89)90181-2, 1989.

520 Carsey, F. D. and Garwood, Jr. R. W.: Identification of modeled ocean plumes in Greenland Gyre ERS-1 SAR data, Geophys. Res. Lett., 20, 2207-2210, doi:10.1029/93GL01954, 1993.

Coleman, G. N., Ferziger, J. H., Spalart, P. R.: A numerical study of the turbulent Ekman layer. Journal of Fluid Mechanics, 213, 313–348, doi:10.1017/S0022112090002348, 1990.

Davis, P. E., and Nicholls, K. W.: Turbulence observations beneath larsen C ice shelf,
525 Antarctica. J. Geophys. Res. Oceans, 124(8), 5529–5550, doi:10.1029/2019JC015164, 2019.

Denbo, D. W. and Skyllingstad E. D.: An ocean large-eddy simulation model with application to deep convection in the Greenland Sea, J. Geophys. Res.,101, 1095–1110, doi:10.1029/95JC02828, 1996.

Derbyshire, S. H.: Nieuwstadt's stable boundary layer revisited. Quart. J. Roy. Meteor. Soc., 116(491), 127–158, 1990.

Dinniman, M. S., Asay-Davis, X. S., Galton-Fenzi, B. K., Holland, P. R., Jenkins, A. and Timmermann, R.: Modeling ice
530 shelf/ocean interaction in Antarctica: A review, Oceanography, 29(4), 144–153, doi:10.5670/oceanog.2016.106, 2016.

Everett, A., Kohler, J., Sundfjord, A., Kovacs, K. M., Torsvik, T., Pramanik, A., Boehme, L. and Lydersen, C.: Subglacial discharge plume behaviour revealed by CTD-instrumented ringed seals, Sci. Rep., 8(1), 13467, doi:10.1038/s41598-018-31875-8, 2018.

Galton-Fenzi, B. K., Hunter, J. R., Coleman, R., Marsland, S. J., Warner, R. C.: Modeling the basal melting and marine ice
535 accretion of the Amery Ice Shelf. J. Geophys. Res. Oceans, 117(C9), doi:10.1029/2012JC008214, 2012.

Garabato, A. C. N., Forryan, A., Dutrieux, P., Brannigan, L., Biddle, L. C., Heywood, K. J., Jeknins, A., Firing, Y. L., Kimura, S.: Vigorous lateral export of the meltwater outflow from beneath an Antarctic ice shelf. Nature, 542(7640), 219–222, doi.org/10.1038/nature20825, 2017.

Gao, X., Dong, C., Liang, J., Yang, J., Li, G., Wang, D. and McWilliams, J. C.: Convective instability-induced mixing and

540 its parameterization using large eddy simulation, Ocean Model., 137, 40–51, 2019, doi:10.1016/j.ocemod.2019.03.008, 2019.

Gayen, B., Griffiths, R. W. and Kerr, R. C.: Simulation of convection at a vertical ice face dissolving into saline water, J. Fluid Mech., 798, 284–298, doi:10.1017/jfm.2016.315, 2016.

Glendening, J. W.: Horizontally integrated atmospheric heat flux from an Arctic lead, J. Geophys. Res., 100, 4613 – 4621, doi: doi:10.1029/94JC02424, 1995.

545 Guest, P. S.: Inside Katabatic Winds Over the Terra Nova Bay Polynya: 1. Atmospheric Jet and Surface Conditions. J. Geophys. Res. Atmos., 126(20), doi:10.1029/2021JD034902, 2021.

Gwyther, D. E., Cougnon, E. A., Galton-Fenzi, B. K., Roberts, J. L., Hunter, J. R., and Dinniman, M. S.: Modelling the response of ice shelf basal melting to different ocean cavity environmental regimes, Ann. Glaciol., 57(73), 131–141, doi:10.1017/aog.2016.31, 2016.

550 Hattermann, T., Nøst, O. A., Lilly, J. M., and Smedsrud, L. H: Two years of oceanic observations below the Fimbul Ice Shelf, Antarctica. Geophysical Research Letters, 39(12), doi:10.1029/2012GL051012, 2012.

Heorton, H. D., Radia, N., and Feltham, D. L.: A model of sea ice formation in leads and polynyas. Journal of Physical Oceanography, 47(7), 1701-1718, doi:10.1175/JPO-D-16-0224.1, 2017.

Hewitt, I. J.: Subglacial Plumes. Annual Review of Fluid Mechanics, 52, 145-169, doi:10.1146/annurev-fluid-010719-

555 060252, 2020.

Horgan, H. J., Walker, R. T., Anandakrishnan, S., & Alley, R. B.: Surface elevation changes at the front of the Ross Ice Shelf: Implications for basal melting. J. Geophys. Res. Oceans, 116, C02005. doi:10.1029/2010JC006192, 2011.

Holland, D. M., Nicholls, K. W. and Basinski, A.: The Southern Ocean and its interaction with the Antarctic Ice Sheet, Science, 367(6484), 1326–1330, doi:10.1126/science.aaz5491, 2020.

560 Holland, D. M. and Jenkins, A.: Modeling thermodynamic ice–ocean interactions at the base of an ice shelf, J. Phys. Oceanogr., 29(8), 1787–1800, doi:10.1175/1520-0485(1999)029<1787:MTIOIA>2.0.CO;2, 1999.

Irwin, J. S.: A theoretical variation of the wind profile power-law exponent as a function of surface roughness and stability. Atmos. Environ. (1967), 13(1), 191–194, doi:10.1016/0004-6981(79)90260-9, 1979.

Jacobs, S. S., Helmer, H. H., Doake, C. S. M., Jenkins, A. and Frolich, R. M.: Melting of ice shelves and the mass balance of

565 Antarctica, J. Glaciol., 38(130), 375–387, doi:10.3189/S0022143000002252, 1992.

Jackett, D. R., Mc Dougall, T. J., Feistel, R., Wright, D. G., Griffies, S. M.: Algortihms for density, potential temperature, conservative temperature, and the freezing temperature of seawater, J. Atmos. Ocean. Tech., 23, 1709–1728, doi:10.1175/JTECH1946.1, 2006.

Jenkins, A.: A simple model of the ice shelf–ocean boundary layer and current. J. Phys. Oceanogr., 46(6), 1785–1803, doi:
10.1175/JPO-D-15-0194.1, 2016.

Jenkins, A., Dutrieux, P., Jacobs, S. S., McPhail, S. D., Perrett, J. R., Webb, A. T. and White, D.: Observations beneath Pine
Island Glacier in West Antarctica and implications for its retreat, Nat. Geosci., 3(7), 468–472, doi:10.1038/ngeo890, 2010

Joughin, I., Alley, R. B. and Holland, D. M.: Ice-Sheet Response to Oceanic Forcing. Science, 338(6111), 1172–1176,
doi:10.1126/science.1226481, 2012.

Kikumoto, H., Ooka, R., Sugawara, H., Lim, J.: Observational study of power-law approximation of wind profiles within an
urban boundary layer for various wind conditions. J. Wind Eng. Ind. Aerod., 164, 13–21, doi:10.1016/j.jweia.2017.02.003,
2017.

Kimura, S., Nicholls, K. W., and Venables, E.: Estimation of ice shelf melt rate in the presence of a thermohaline staircase. J.
Phys. Oceanogr., 45(1), 133–148, doi:10.1175/JPO-D-14-0106.1, 2015.

Li, B. R., Wang, M. M., Lu, X. Y., Wan, Z. H. and Song, H. E.: Effect of Salinity on Sea Ice Motion. Therm. Sci., 22(4),
1563–1570, doi:10.2298/TSCI1804563L, 2018.

Liu, Y., Moore, J. C., Cheng, X., Gladstone, R. M., Bassis, J. N., Liu, H., et al.: Ocean-driven thinning enhances iceberg
calving and retreat of Antarctic ice shelves. Proc. Natl. Acad. Sci. 112, 3263–3268, doi:10.1073/pnas.1415137112, 2015.

Maronga, B., Gryschka, M., Heinze, R., Hoffmann, F., Kanani-Sühring, F., Keck, M., Ketelsen, K., Letzel, M. O., Sühring.
M. and Raasch, S.: The Parallelized Large-Eddy Simulation Model (PALM) version 4.0 for atmospheric and oceanic flows:
model formulation, recent developments, and future perspectives, Geosci. Model Dev., 8, 2515–2551, doi:10.5194/gmdd-8-
1539–2015, 2015.

Matsumura, Y. and Ohshima, K. I.: Lagrangian modelling of frazil ice in the ocean, Ann. Glaciol., 56(69) 373–382,
doi:10.3189/2015AoG69A657, 2015.

McPhee, M. G., Maykut, G. A. and Morison, J. H.: Dynamics and thermodynamics of the ice/upper ocean system in the
marginal ice zone of the Greenland Sea, J. Geophys. Res., 92, 7017–7031, doi:10.1029/JC092iC07p07017, 1987.

McConnochie, C. D., and Kerr, R. C.: Dissolution of a sloping solid surface by turbulent compositional convection. J. Fluid
Mech, 846, 563–577, doi:10.1017/jfm.2018.282, 2018.

Mondal, M., Gayen, B., and Kerr, R.: Ablation of sloping ice faces into polar seawater. J. Fluid Mech, 863, 545–571,
doi:10.1017/jfm.2018.970, 2019

Nicholls, K. W., Abrahamsen, E. P., Buck, J. J. H., Dodd, P. A., Goldblatt, C., Griffiths, G., Heywood, K. j., Hughes, N. E.,
Kalezky, A., Lane-Serff, G. F., McPhail, S. D. Millard, N. W., Oliver, K. I. C., Perrett, J., Price, M. R., Pudsey, C. J., Saw, K,
Stansfield, K., Stott, M. J., Wadhams, P., Webb, A. T. and Wilkinson, J. P.: Measurements beneath an Antarctic ice shelf using
an autonomous underwater vehicle, Geophys. Res. Lett., 33(8), doi:10.1029/2006GL025998, 2016.

Noh, Y., Goh, G., Raasch, S. and Gryschka, M.: Formation of a diurnal thermocline in the ocean mixed layer simulated by
LES, J. Phys. Oceanogr., 39(5), 1244–1257, doi:10.1175/2008JPO4032.1, 2009.

Pope, S. B.: Turbulent flows, 2001.

Raasch, S. and Schröter, M.: PALM–a large-eddy simulation model performing on massively parallel computers, Meteorol. Z., 10(5), 363–372, doi:10.1127/0941-2948/2001/0010-0363, 2001.

605 Ramudu, E., Gelderloos, R., Yang, D., Meneveau, C. and Gnanadesikan, A.: Large eddy simulation of heat entrainment under arctic sea ice, J. Geophys. Res. Oceans, 123, 287–304, doi:10.1002/2017JC013267, 2018.

Rees Jones, D. W., Wells, A. J.: Frazil-ice growth rate and dynamics in mixed layers and sub-ice-shelf plumes. Cryosphere, 12(1), 25–38, doi:10.5194/tc-12-25-2018, 2018.

Rignot, E., Jacobs, S., Mouginot, J. and Scheuchl, B.: Ice-shelf melting around Antarctica, Science, 341(6143), 266–270,
610 doi:10.1126/science.1235798, 2013.

Rygg, K., Alendal, G. and Haugan, P. M.: Flow over a rounded backward-facing step, using az-coordinate model and a σ-coordinate model. Ocean Dynamics, 61(10), 1681-1696, doi:10.1007/s10236-011-0434-3, 2011.

SeaBird Electronics, Inc.: Seasoft V2: SBE data processing (User's Manual, pp. 1–174). Bellevue, Washington, USA, 2014.

Sharqawy, M. H., Lienhard, J. H. and Zubair, S. M.: Thermophysical properties of seawater: a review of existing correlations
615 and data. Desalination and water treatment, 16(1–3), 354–380, doi:10.5004/dwt.2010.1079, 2010.

Skyllingstad, E. D. and Denbo, D. W.: Turbulence beneath sea ice and leads: a coupled sea ice/large eddy simulation study, J. Geophys. Res., 106(C2), 2477–2497, doi:10.1029/1999JC000091, 2001.

Smedsrud, L. H. and Jenkins, A.: Frazil ice formation in an ice shelf water plume. J. Geophys. Res., 109(C3), doi:10.1029/2003JC001851, 2004.

620 Smith, B., Fricker, H. A., Gardner, A. S., Medley, B., Nilsson, J., Paolo, F. S., Holschuh, N., Adusumilli, S., Brunt, K., Csatho, B., Harbeck, K., Markus, T., Neumann, T., Siegfried, M. R., and Zwally, H. J.: Pervasive ice sheet mass loss reflects competing ocean and atmosphere processes. Science, eaaz5845, doi:10.1126/science.aaz5845, 2020.

Smethie Jr, W. M., & Jacobs, S. S. Circulation and melting under the Ross Ice Shelf: estimates from evolving CFC, salinity and temperature fields in the Ross Sea. Deep-Sea Res. I: Oceanogra. Res. Pap., 52(6), 959–978, doi: 10.1016/j.dsr.2004.11.016,
625 2005

Stanton, T. P., Shaw, W. J., Truffer, M., Corr, H. F. J., Peters, L. E., Riverman, K. L., Bindschadler, R., Holland, D. M., and Anandakrishnan, S.: Channelized Ice Melting in the Ocean Boundary Layer Beneath Pine Island Glacier, Antarctica. Science, 341(6151), 1236–1239, doi: 10.1126/science.1239373, 2013.

Stevens, C., Lee, W. S., Fusco, G., Yun, S., Grant, B., Robinson, N. and Hwang, C. Y.: The influence of the Drygalski Ice
630 Tongue on the local ocean, Ann. Glaciol., 58(74), 51–59, doi:10.1017/aog.2017.4, 2017.

Thompson, L., Smith, M., Thomson, J., Stammerjohn, S., Ackley, S., and Loose, B.: Frazil ice growth and production during katabatic wind events in the Ross Sea, Antarctica. Cryosphere, 14(10), 3329–3347, doi:10.5194/tc-14-3329-2020, 2020.

Thurnherr, A. M.: How to Process LADCP Data with the LDEO Software. New York: Columbia University. ftp://ftp.ldeo.columbia.edu/pub/LADCP/HOWTO/LDEO_IX.pdf, 2014.

635 Vreugdenhil, C. A., and Taylor, J. R.: Stratification effects in the turbulent boundary layer beneath a melting ice shelf: Insights from resolved large-eddy simulations, J. Phys. Oceanogr., 49(7), 1905–1925, doi:10.1175/JPO-D-18-0252.1, 2019.

Wicker, L. J. and Skamarock, W. C.: Time-splitting methods for elastic models using forward time schemes, Mon. Weather Rev., 130(8), 2088–2097, doi:10.1175/1520-0493(2002)130<2088:TSMFEM>2.0.CO;2, 2002.

Wray, P. A.: Spatial analysis of the Nansen ice shelf basal channel, using ice penetrating radar (Master's thesis, University of Waterloo), 2019.

Yoon, S. T., Lee, W. S., Stevens, C., Jendersie, S., Nam, S., Yun, S., Hwang, C. Y., Jang, G. I., and Lee, J.: Variability in high-salinity shelf water production in the Terra Nova Bay polynya, Antarctica, Ocean Sci., doi:10.5194/os-16-373-2020, 2020.

645   **Table 1. List of model parameters and constants**

λ_1	Freezing temperature salinity coefficient	-0.0573	°C kg g^{-1}
λ_2	Freezing temperature constant	0.0832	°C
λ_3	Freezing temperature depth coefficient	-7.53×10^4	°C m^{-1}
Γ_S	Salt turbulent transfer coefficient (sea surface, ice shelf bottom)	2×10^{-4} [a], 2.6×10^{-4} [b]	-
Γ_θ	Heat turbulent transfer coefficient (sea surface, ice shelf bottom)	5.8×10^{-3} [a], 8×10^{-3} [b]	-
c_w	Specific heat capacity of pure water	3974	J kg^{-1}°C^{-1}
L_i	Latent heat of fusion	3.35×10^5	J kg^{-1}
ρ_w	Density of water	1028	kg m^{-3}
ρ_i	Density of ice	917	kg m^{-3}
z_0	Surface roughness (sea surface, ice shelf bottom)	0.001, 0.005[c]	m
-	Ice shelf thickness	280[d]	m
θ_f	Local freezing temperature (sea surface, ice shelf bottom)	$-1.9, -2.115$	°C
θ_a	Ambient temperature (sea surface, ice shelf bottom)	$-1.9, -2.06$	°C
θ_b	Interfacial temperature (sea surface, ice shelf bottom)	$-1.879, -2.092$	°C
Sa_a	Ambient salinity (sea surface & ice shelf bottom)	34.69	Psu
Sa_b	Interfacial salinity (sea surface, ice shelf bottom)	34.9425, 34.286	Psu
k_θ	molecular diffusivities of heat	1.3×10^{-7}	m^2 s^{-1}
k_S	molecular diffusivities of salt	7.2×10^{-10}	m^2 s^{-1}
u_*	Friction velocity (sea surface, ice shelf bottom)	0.026, calculated	m s^{-1}
	Wind speed, air temperature in AWS	16.23, -7.76	m s^{-1}, °C
Q_s	Sensible heat flux at sea surface	164.88[e]	W m^{-2}
F	Sea-ice formation	1.38[e]	cm day^{-1}

a – Heorton et al. (2017)

b – based on friction velocity (0.168 m s^{-1}) and thermal driving (refer to Vreugdenhil and Taylor (2019))

c – Smooth ice with melting case (C$_d$ = 0.001) in Gwyther et al. (2016)

d – Stevens et al. (2017)

e – Thompson et al. (2020)

Table 2. Main values of four different cases ($Ri_f = \frac{\frac{g}{\rho_{\theta,0}}(\overline{\rho_\theta' w'})}{-\overline{u'w'}(\frac{\partial U_x}{\partial z})}$)

Case	Friction velocity at ice shelf (m s^{-1})	IOBL depth (m)	Large eddy turnover time, t* (hour)	Averaged melt rate (m yr^{-1})	Averaged freezing rate (m yr^{-1})	Flux Richardson number, Ri_f
n=3	0.001686	30	4.94	0.092	2.628	0.0464
n=4	0.002077	33	4.41	0.109	2.72	0.0418
n=5	0.002548	36	3.93	0.139	2.671	0.0599
n=7	0.002765	39	3.92	0.153	3.142	0.0378
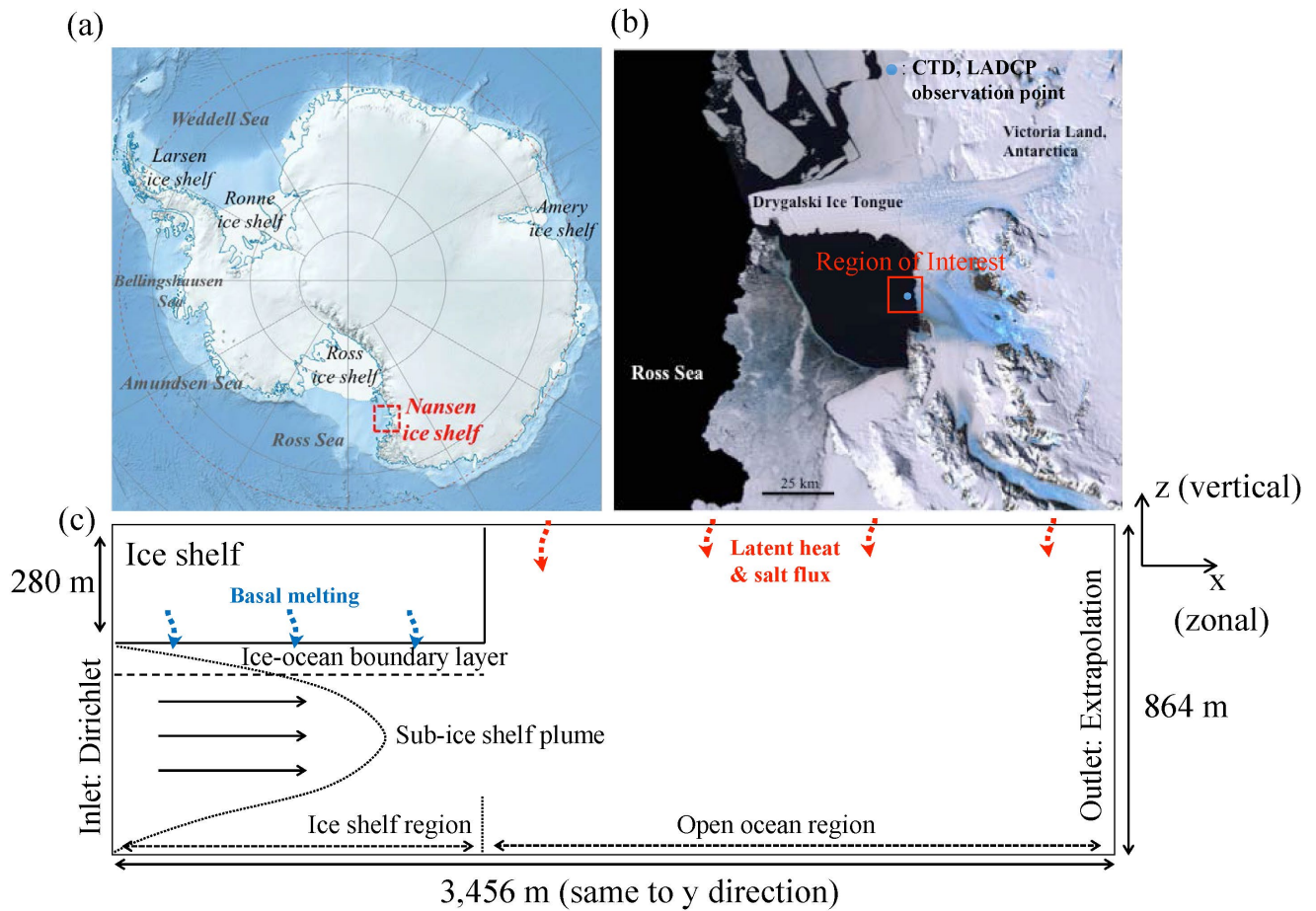
Figure 1: Region of interest and simulation domain configuration. (a) Map of Antarctica. The red box shows the study are, Terra Nova Bay, in the western Ross Sea. (b) Region of interest where the CTD and LADCP surveys were conducted in the 2016–17 shipboard survey. (c) Simulation domain and boundary conditions.
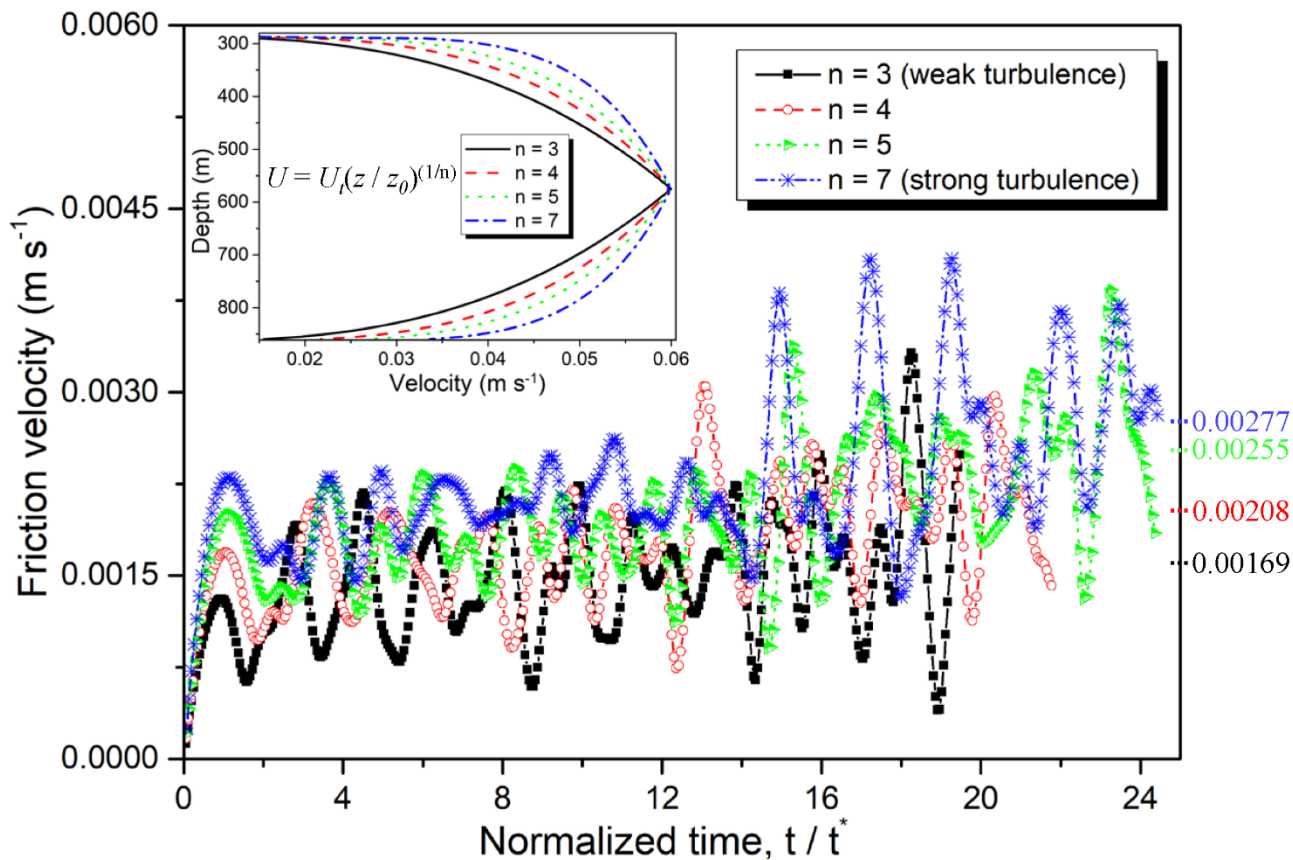
Figure 2: Time series of the friction velocities in all the four cases. The total time (96 h) was normalized by each large-eddy turnover time, t*, which was calculated from the overturning eddy scale (ice shelf-ocean boundary layer (IOBL) scale) divided by the friction velocity. The inset figure shows four different theoretical profiles of the velocity.

660
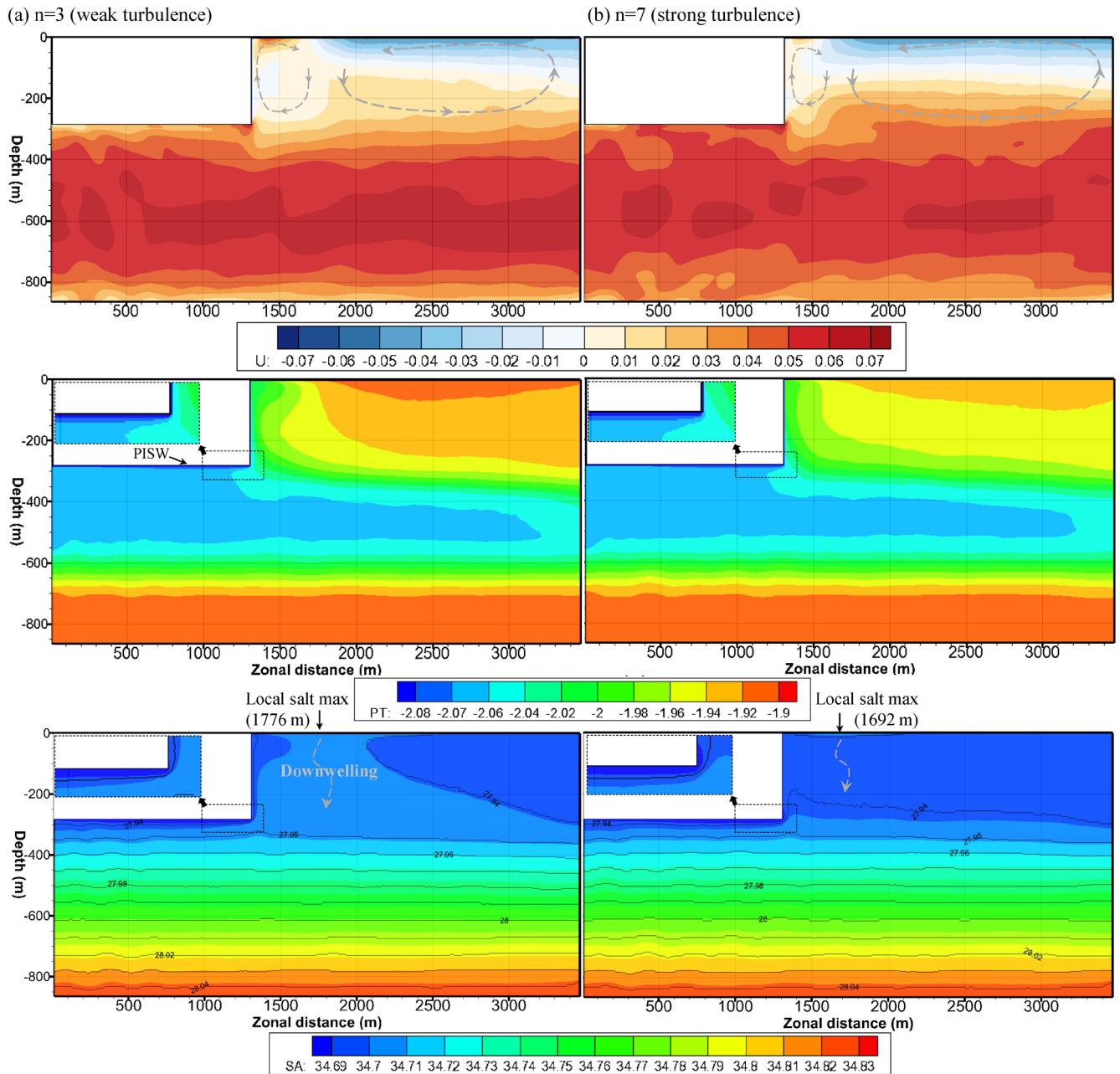
Figure 3: XZ cross-sectional contours (y = 1,728 m, domain center) of the zonal velocity, potential temperature, and salinity in the n = 3 (left) and n = 7 (right) cases. In these contours, the zonal direction is perpendicular to the ice shelf front. These results are time-averaged in the last 3 t* period. Upper panel: zonal velocity, middle panel: potential temperature, and lower panel: salinity. In the lower panel, the isopycnal lines are identified by the potential density (kg m⁻³) with 0.01 intervals.
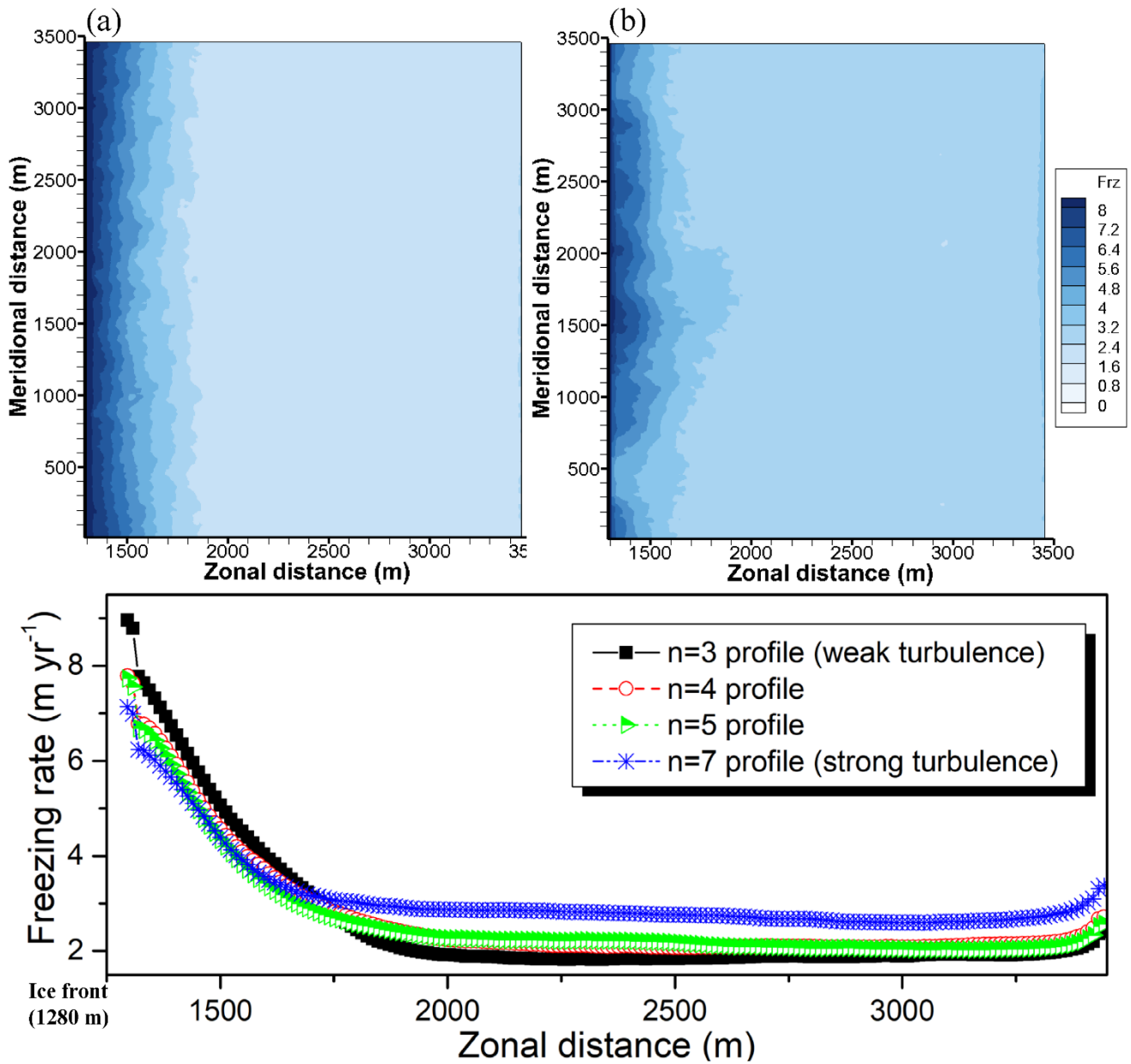
Figure 4: XY horizontal distribution of the 3 t* time-averaged freezing rate (m yr⁻¹) at the sea surface. (a) n = 3, weak turbulence. (b) n = 7, strong turbulence (c) Zonal-spatial distribution of the freezing rate in the four different turbulence cases. These values are averaged along the meridional direction.
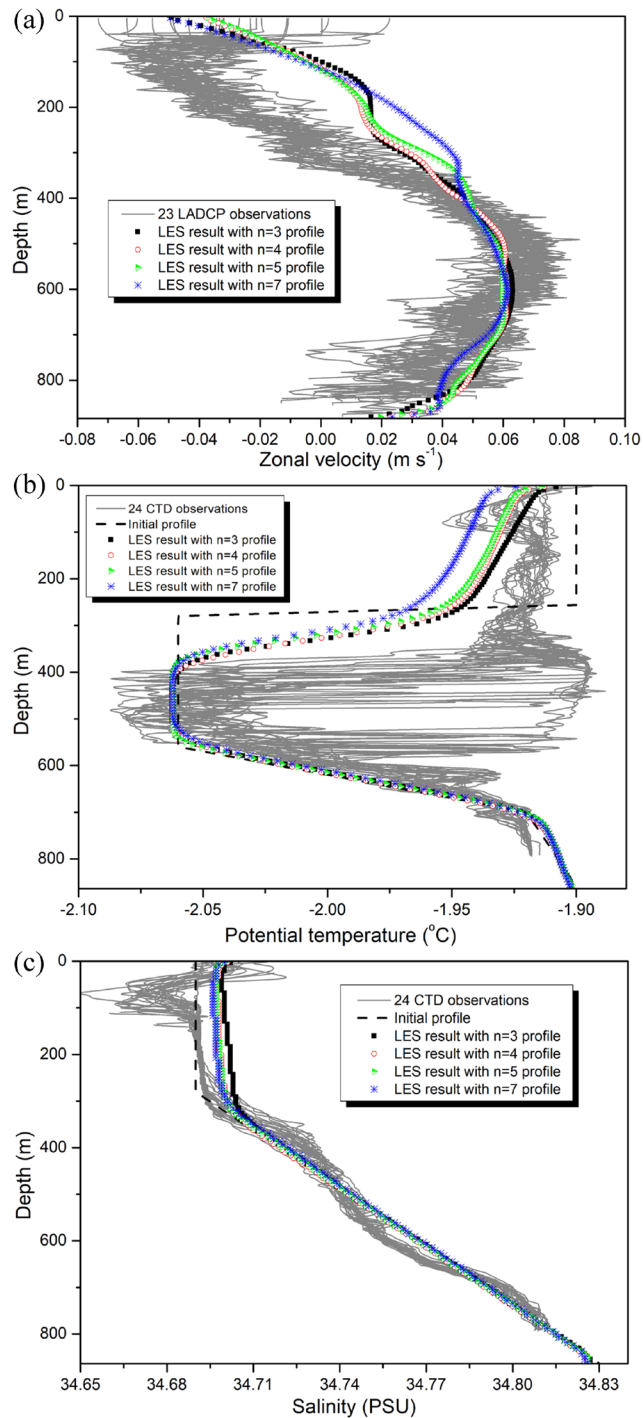
Figure 5: Vertical profiles of the velocity, potential temperature, and salinity obtained from the CTD and LADCP observational data (solid grey lines), initial profiles (black dashed line), and the results of the large-eddy simulation (LES). (a) zonal velocity; (b) potential temperature; (c) salinity.
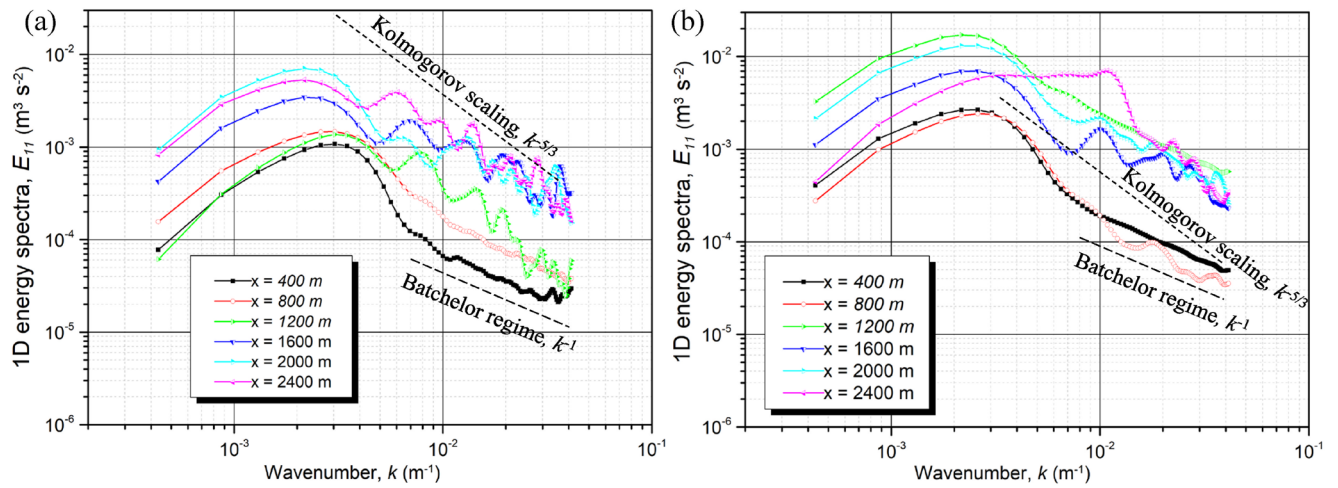
680

Figure 6: One-dimensional turbulence energy spectra at a depth of 291 m at the PISW within the IOBL. (a) n = 3 and (b) n = 7. Different shapes and colors represent the values at different zonal distances: 400, 800, 1200, 1600, 2000 and 2400 m. These power spectra are obtained by y-direction (meridional direction) spatial assessment of time-averaged velocity at each x location. The –5/3 slope (Kolmogorov scaling) represents the regime of inertial subrange, whereas –1 slope (Batchelor) represents viscous-convective
685 **range in high-Schmidt number.**
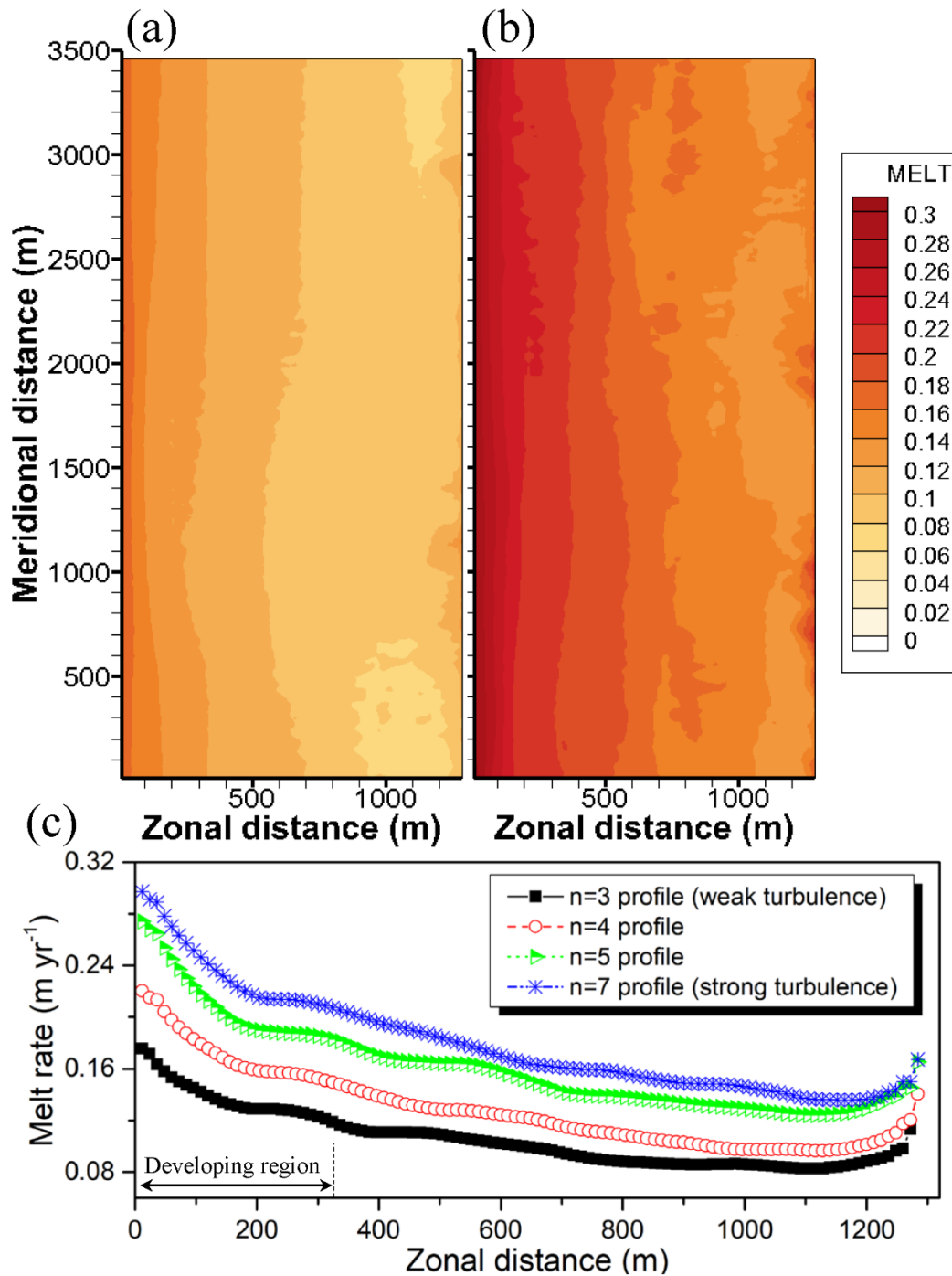
Figure 7: XY horizontal distribution of 3 t* time-averaged melt rate (m yr⁻¹) at the ice shelf base (280 m). (a) n = 3, weak turbulence. (b) n = 7, strong turbulence (c) Zonal-spatial distribution of the melt rate in four different turbulence cases. These values are averaged along the meridional direction.
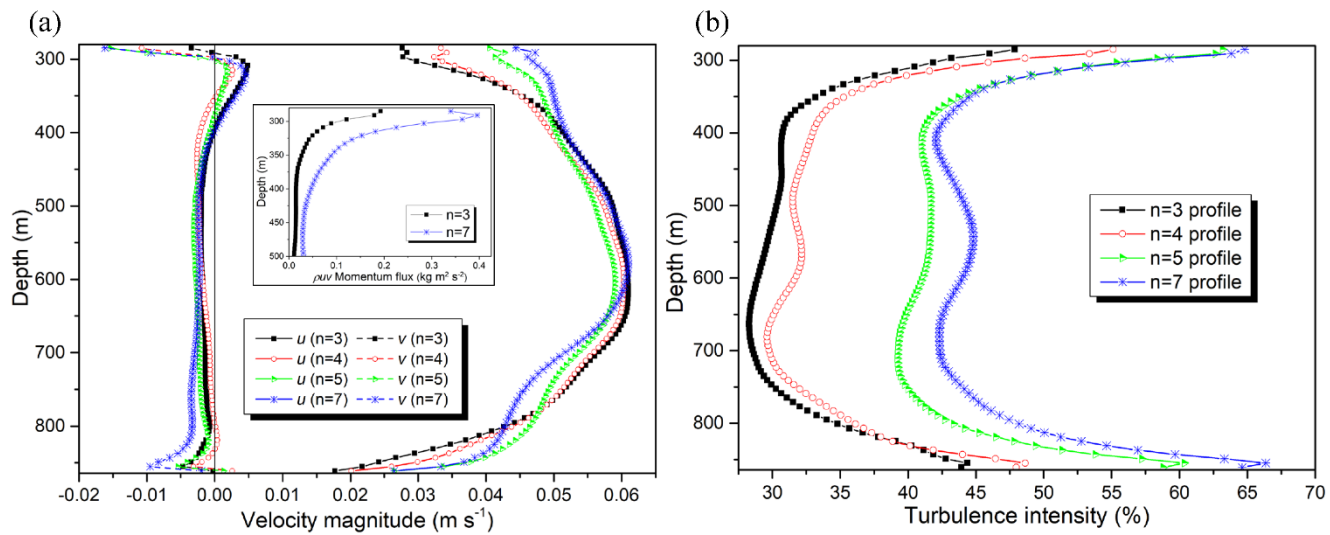
Figure 8: Vertical profiles of (a) *u*, *v* mean velocities and (b) turbulence intensity. The inset in (a) shows the vertical profile of the horizontal momentum flux for the Ekman layer formation beneath the ice shelf.

695

700
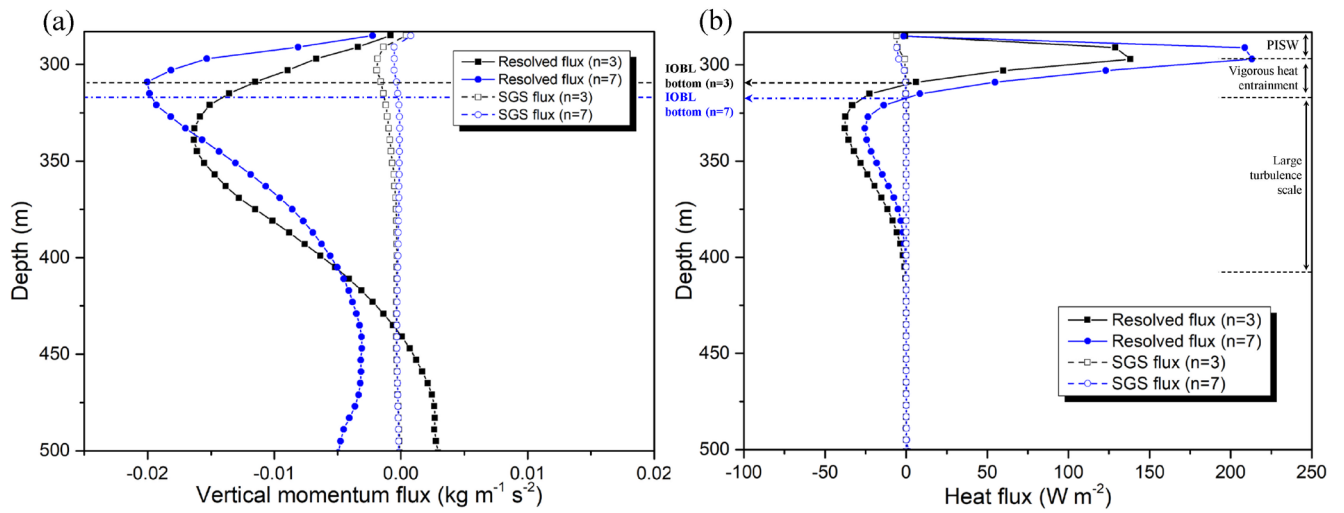
705 **Figure 9: Vertical profiles of the momentum fluxes and heat fluxes. The fluxes were characterized using resolved flux and subgrid scale (SGS) flux. (a) Momentum fluxes (resolved: $\rho_0\overline{u'w'}$, SGS: $\rho_0 K_m \overline{\partial u/\partial z}$). (b) Heat fluxes (resolved: $\rho_0 c_s \overline{w'\theta'}$, SGS: $\rho_0 c_s K_h \overline{\partial \theta/\partial z}$, where ρ_0 (1024 kg m^{-3}) is the reference density of seawater, and c_s (4.02 × 10^3 J kg^{-1} K^{-1}) is the specific heat capacity of seawater (Sharqawy et al., 2010)).**

710
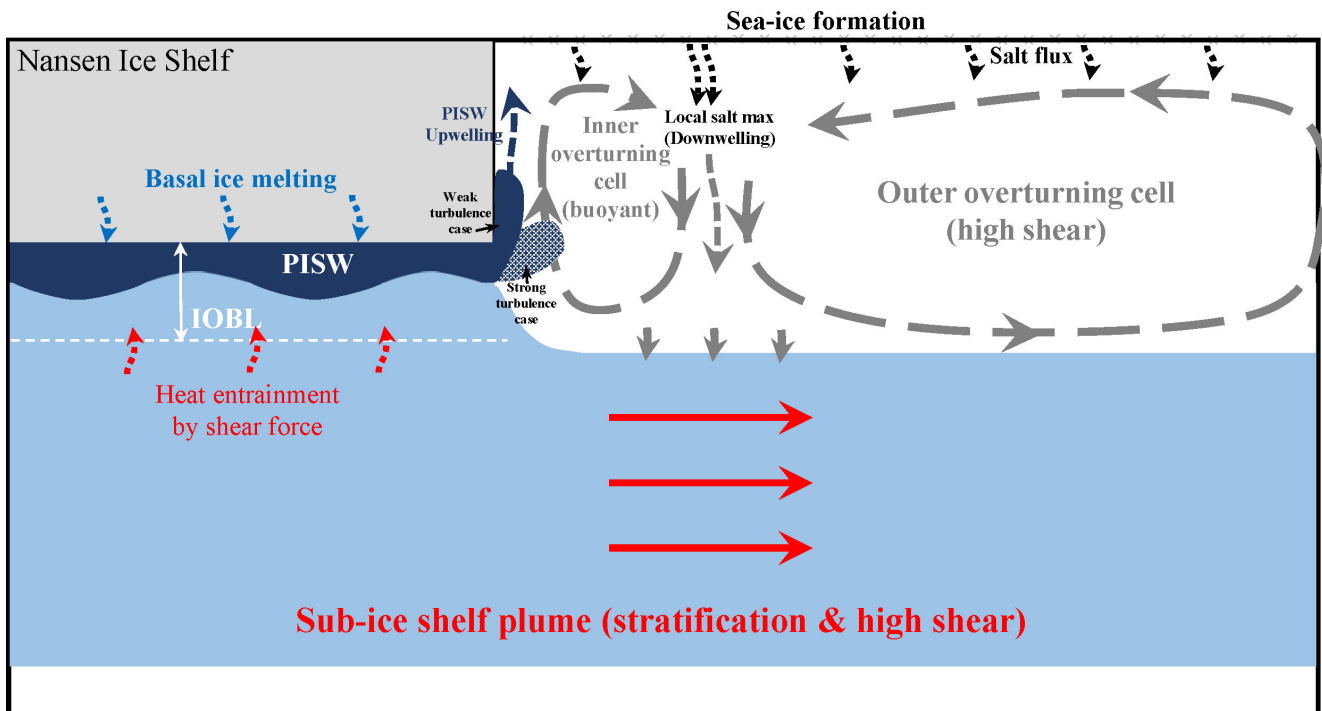
Figure 10: Final conclusions and schematic diagram representing the oceanographic picture near the NIS front and the various phenomenon that occur within the IOBL, as resolved via LES.